



RADBOUD UNIVERSITEIT NIJMEGEN

*A thesis submitted in fulfilment of the requirements  
for the degree of MASTERS OF SCIENCE*

---

# Enhancing Solar Cell Efficiency with a Ferroelectric Polymer and Temperature Dependent Surface Photovoltage

---

*Research carried out at  
The Weizmann Institute of Science*

*Author:*

Timo BRETTEN

*Supervisors:*

Prof. Dr. David CAHEN  
Dr. Hugo MEEKES

November 26, 2015

*“The most dangerous world view is that of those who have not viewed the world.”*

Alexander von Humboldt

# Contents

|  |           |
|--|-----------|
| <b>1 Enhancing Solar Cell Efficiency with a Ferroelectric Polymer</b>                  | <b>1</b>  |
| 1.1 Introduction and Motivation . . . . .  | 2         |
| 1.2 Ferroelectricity . . . . .   | 3         |
| 1.3 Polyvinylidene Difluorite and its Copolymers . . . . .                             | 5         |
| 1.3.1 P(VDF) Nanoparticles . . . . .   | 8         |
| 1.4 Experimental Techniques . . . . .  | 10        |
| 1.4.1 Contact Potential Difference and Surface Photovoltage . . . . .                  | 10        |
| 1.4.2 Determination of Excess Carrier Lifetimes . . . . .                              | 10        |
| 1.4.3 Infrared Spectroscopy . . . . .  | 12        |
| 1.4.4 Ellipsometry and Contact Profilometry . . . . .                                  | 13        |
| Ellipsometry . . . . .   | 13        |
| Contact Profilometry . . . . .   | 13        |
| 1.4.5 Electron Microscopy . . . . .  | 14        |
| 1.4.6 IV-Curves . . . . .  | 14        |
| 1.4.7 Dynamic Light Scattering . . . . .   | 15        |
| 1.5 Experimental Approach, Results and Discussion . . . . .                            | 16        |
| 1.5.1 Sample Preparation . . . . .   | 16        |
| Si–H Substrates . . . . .  | 16        |
| P(VDF-TrFE 70:30) Thin Films . . . . .   | 17        |
| P(VDF-TrFE 70:30) Nanoparticles . . . . .  | 18        |
| 1.5.2 CPD SPV . . . . .  | 19        |
| Standard Experiments . . . . .   | 19        |
| Pole-Reverse-Pole . . . . .  | 19        |
| 1.5.3 Lifetimes . . . . .  | 19        |
| 1.5.4 Ellipsometry . . . . .   | 19        |
| 1.5.5 IR . . . . .   | 19        |
| 1.5.6 IV . . . . .   | 19        |
| 1.5.7 Scanning Electron Microscopy . . . . .   | 19        |
| Influence of Solvent on Thin Film Morphology . . . . .                                 | 19        |
| Nanoparticle characterisation . . . . .  | 21        |
| 1.5.8 DLS . . . . .  | 23        |
| 1.6 Discussion . . . . .   | 23        |
| <b>2 Temperature Dependent Surface Photovoltage</b>                                    | <b>24</b> |
| 2.1 Introduction . . . . .   | 25        |
| 2.2 Theory . . . . .   | 25        |
| 2.2.1 The Contact Potential Difference and the Kelvin Probe . . . . .                  | 25        |
| 2.2.2 The Surface Photovoltage and Band Bending . . . . .                              | 27        |
| 2.3 Kelvin Probes in use . . . . .   | 29        |
| 2.3.1 Established Kelvin Probe System . . . . .  | 29        |
| 2.3.2 The Lakeshore Cryogenic System coupled with a Mc Allister Kelvin Probe . . . . . | 30        |

|       |  |           |
|-------|--|-----------|
| 2.4   | Measuring CPD at room temperature . . . . .  | 33        |
| 2.4.1 | Sample Preparation . . . . .   | 33        |
| 2.4.2 | Results & Discussion . . . . .   | 33        |
| 2.5   | CPD as function of pressure and temperature . . . . .                                    | 34        |
| 2.5.1 | CPD as a function of pressure . . . . .  | 34        |
| 2.5.2 | CPD as a function of temperature . . . . .   | 36        |
| 2.5.3 | Conclusion . . . . .   | 36        |
| 2.6   | Measuring the SPV at room temperature . . . . .  | 36        |
| 2.7   | Temperature dependent measurement of the SPV . . . . .                                   | 39        |
| 2.7.1 | Vanadium oxide . . . . .   | 40        |
|       | Description of samples and preliminary research carried out at the Cahen group . . . . . | 40        |
|       | Experimental procedure, results and discussion . . . . .                                 | 41        |
| 2.8   | Conclusion . . . . .   | 45        |
|       | <b>List of References</b>  | <b>47</b> |

# List of Figures

|      |   |    |
|------|---|----|
| 1.1  | Schematic polarisation plots for different types of materials. . . . .  | 4  |
| 1.2  | Schematic representation of the structural phases in a ferroelectric at a temperature above the Curie temperature (1.2a), below the Curie temperature (1.2b) and below the Curie temperature in the presence of an external electric field (1.2c). Adopted from Kittel [1, p. 478]. . . . .   | 5  |
| 1.3  | An approximate chemical structure for P(VDF-TrFE 70:30). The direction of the dipole moment, from Hydrogen to Fluorine, is indicated. . . . .   | 5  |
| 1.4  | Along-the-chain and top down views of ball and stick models for two crystalline forms of pure P(VDF). Fluorine atoms are green, carbon black, hydrogen grey. Adopted from [2, p. 809]. . . . .  | 6  |
| 1.5  | Fischer-Projections and internal energy as a function of the torsion angle along the chain. The minimum at 180° corresponds to the <i>trans</i> $\beta$ -phase. Adopted from [2, p. 809]. . . . .   | 7  |
| 1.6  | Schematic representations of the unit cells of two crystalline phases of P(VDF). Fluorine atoms are green, carbon black, hydrogen grey. The direction of the dipole moment in the $\beta$ -phase is indicated. Adopted from [2, pp. 809 f.]. . . . .  | 8  |
| 1.7  | Effect of annealing temperature on remnant polarisation $P_r$ and degree of crystallinity in P(VDF-TrFE) with a TrFE content of 32 mol %, adopted from [2, p. 813]. The line through the data points was constructed with a spline fit and is not based on a physical model. . . . .  | 9  |
| 1.8  | Schematic of an ATR FTIR set-up. Figure 1.8a shows the internal reflection of the beam of light at the edges of the guiding crystal (light gray) and the thin film sample (yellow) on its substrate (dark grey) being pressed onto the crystal. Figure 1.8b focuses on the evanescent wave projecting into the thin film and gives an indication how the beam, while being nominally inside the crystal, can still be attenuated by the sample. Adopted from VILAN. . . . . | 12 |
| 1.9  | A schematic of a typical, simplified DLS set-up. Figure 1.9a shows the main components: (laser) source, sample cell, detectors, auto-correlator and a computer for data-sampling. Two detectors allow for measurement of relative intensity and thus help reduce unwanted noise from fluctuations in laser intensity. Figure 1.9b shows how different particle sizes lead to different ‘noise’ signatures in the measured signal. . . . .                                   | 15 |
| 1.10 | SEM images comparing the P(VDF) thin film morphologies obtained from spin casting of different solutions. . . . .   | 20 |
| 1.11 | SEM images comparing ‘normal’ P(VDF) NPs to those that were annealed at $T_C$ on a substrate. . . . .   | 22 |

|      |   |    |
|------|---|----|
| 2.1  | Band bending, trapped surface charges and the space charge region at the surface of an n-type semiconductor (a) in the dark and (b) under illumination. Note the decrease in trapped surface charges in (b) and the resulting reduction in band bending. Energy levels of the valence band, $E_v$ , the Fermi level, $E_f$ , and the conduction band, $E_c$ , are included for reference. . . . .   | 27 |
| 2.2  | Definition of terms electron affinity, $E_{EA}$ , band-bending $\zeta$ , conduction band edge, $E_c$ , Fermi level, $E_f$ and work function, $\varphi$ , for an n-type semiconductor (a) and a p-type semiconductor (b). It can be clearly seen that the band bending is negative for the p-type semiconductor. Valence band edge, $E_v$ , included for reference. . . . .  | 28 |
| 2.3  | Schematic of the Lakeshore model TTPX cryogenic system and its components, typical operational temperatures are indicated. Taken from the vendor's website [3]. . . . .   | 31 |
| 2.4  | Typical relative spectral intensity of the LEDEngine LED at an operating temperature of 25 °C, taken from the vendor's supplementary information [4, p. 10]. . . . .  | 32 |
| 2.5  | Summary of the calculated work functions for the n-Si-H samples used. There is good agreement between the different systems and good agreement with theory, except for the case of low resistivity, highly doped silicon. Indicated errors include deviations in the samples & the inaccuracy of calibration with HOPG. . . . .   | 34 |
| 2.6  | Raw data obtained from a measurement of the CPD during pressure reduction in the Mc Allistercryogenic system. Figure 2.6a shows results obtained from independent measurements of a piece of HOPG carried out on different days. It is indicated which pump was active to reduce the pressure inside the sample chamber. Figure 2.6b gives more detail about one of these measurements and actual measurements of the pressure at different stages during evacuation. . . . .   | 35 |
| 2.7  | Comparison of the measured SPV as a function of illumination level as evidenced by the current through the LED. 'Upstairs' refers to the combination of LED and the ambient probe station, while 'Downstairs' refers to measurements with the LED, the Mc Allister cryostation and the custom Lakeshore KP probe head. 'Old' signifies the weaker, damaged LED of nominally 4200 lm intensity, while 'new' refers to the fully functional LED of 5400 lm intensity. Note that the measurement saturates independent of illumination intensity ('old' vs. 'new') at a lower measured SPV than the comparison with the ambient probe station. . . . . | 38 |
| 2.8  | Raw data of the contact potential difference of the W:VO <sub>2</sub> sample obtained during a temperature-sweep. Data points in red were obtained while cooling down, data points in black were recorded while warming up. . . .   | 42 |
| 2.9  | The contact potential difference of the W:VO <sub>2</sub> sample as a function of temperature. Experimental uncertainties are explained in the text. . . .  | 43 |
| 2.10 | Measured surface photovoltage and calculated work function for the W:VO <sub>2</sub> sample as a function of temperature. The appearance of an SPV coincides with the MIT temperatures observed in earlier measurements, its positive sign indicates an n-type semiconductor. The change in WF is substantial but remains unexplained without further experiments. Experimental uncertainties are explained in the text. . . . .  | 44 |

# List of Tables

|     |  |    |
|-----|--|----|
| 1.1 | Experimental Lattice Dimensions and Angles of pure P(VDF) ( $\alpha$ and $\beta$ ) and of P(VDF-TrFE) ( $\beta$ ) of varying molar ratio. Compiled from [2, p. 810].   | 7  |
| 1.2 | Degree of crystallinity, melting temperature $T_m$ , phase transition temperature $T_C$ , remnant polarisation $P_r$ and coercive field $E_C$ for P(VDF-TrFE) copolymers of varying molar ratio. Some values are approximations because data was visually compiled from figures [2, pp. 812 f.] . . . . .                          | 8  |
| 1.3 | Nanoparticle diameters as obtained by SEM. Values for Xiao <i>et al.</i> are estimated from [9, Figure 1f)]. Batches b <sub>1</sub> through b <sub>3</sub> were refluxed before size determination, batches b <sub>1</sub> & b <sub>2</sub> were centrifuged at 16 500 rpm, b <sub>3</sub> & b <sub>4</sub> at 18 000 rpm. . . . . | 21 |

# List of Abbreviations

|                    |   |
|--------------------|---|
| <b>ATR</b>         | Attenuated Total Reflectance                        |
| <b>BFS</b>         | Back Surface Field                                  |
| <b>CPD</b>         | Contact Potential Difference                        |
| <b>DLS</b>         | Dynamic Light Scattering                            |
| <b>FTIR</b>        | Fourier Transform Infra Red                         |
| <b>HOPG</b>        | Highly Ordered Pyrolytic Graphite                   |
| <b>IR</b>          | Infrared  |
| <b>KP</b>          | Kelvin Probe  |
| <b>LB</b>          | Langmuir-Blodgett                                   |
| <b>LED</b>         | Light Emitting Diode                                |
| <b>MIT</b>         | Metal Insulator Transition                          |
| <b>NP</b>          | Nanoparticle  |
| <b>OPVs</b>        | Organic Photovoltaic cells                          |
| <b>PCB</b>         | Printed Circuit Board                               |
| <b>P(VDF)</b>      | Polyvinylidene Difluoroethylene                     |
| <b>P(VDF-TrFE)</b> | Polyvinylidene Difluoro-Trifluoroethylene copolymer |
| <b>SEM</b>         | Scanning Electron Microscopy                        |
| <b>SPS</b>         | Surface Photovoltage Spectroscopy                   |
| <b>SPV</b>         | Surface Photovoltaic                                |
| <b>SRC</b>         | Space Charge Region                                 |
| <b>TEM</b>         | Transmission Electron Microscopy                    |
| <b>TrFE</b>        | Trifluoroethylene                                   |
| <b>UHV</b>         | Ultra High Vacuum                                   |
| <b>UV</b>          | Ultraviolet   |
| <b>WF</b>          | Work Function                                       |

*Dedicated to my family who thankfully pushed me on.  
Willing or not.*

## Chapter 1

# Enhancing Solar Cell Efficiency with a Ferroelectric Polymer

## 1.1 Introduction and Motivation

The goal of this part of the project was to see whether a well known ferroelectric polymer could be used to enhance the efficiency of solar cell when applied as a thin film to its surface.

Solar cells convert light energy directly into electrical energy via the photoelectric effect and thus they are a proven method for obtaining sustainable energy. Significant amounts of research effort are put into exploring new materials and their possibilities as well as into improving existing types of solar cells. REF Broadly, one can divide the research approaches of solar energy conversion into two main categories: either a high quality, high cost approach that tries to maximise ultimate efficiencies as much as possible or a ‘low’ quality, low cost approach that tries to strike an advantageous balance between production costs and obtained efficiency. The former is, for example, represented by complex III-IV multi-junction solar cells that maximise the usage of the available solar spectrum in each of their layers separately. REF Efficiencies as high as XXX0 % have been reported REF and even higher efficiencies may be reached when utilising light-concentrator schemes<sup>1</sup> REF. The second approach focuses more on new materials or tries to combine the advantages of wet-chemical production processes, namely their versatility and low cost, with solar cell preparation. Here, the Cahen group has made significant advances by showing how molecular surface modifications can be used to improve the efficiency of existing cells and by demonstrating a silicon inversion-layer type solar cell where the inversion layer is created by, again, molecular surface modifications REF. To explain a little further: in a ‘typical’ silicon solar cell a p-n-junction is created by changing the type of dopant introduced into molten silicon during cell growth. This process is relatively costly in terms of energy and, accordingly, in terms of money as well. In an inversion-layer type solar cell, on the other hand, only one type of material (either p- or n-type doped silicon) is used and the necessary junction is formed by excluding one type of charge carriers in a thin layer directly the cell surface by a strong electric field created by chemisorbed dipolar molecules. In this respect, the attempt at creating a comparable effect by a physisorbed ferroelectric polymer is a logical continuation of ongoing work in the Cahen group. Furthermore, one significant loss mechanism in solar cells is unwanted surface recombination of created charge carriers. The efficiency of this loss mechanism is dependent on the product of the two types of charge carriers and therefore, if one type of charge carrier can be excluded from the surface, a reduction of losses is expected. Similar approaches are realised by, for example, including a back-surface field (BFS) in industrially grown silicon solar cells REF. The ferroelectric polymer of choice has also been implemented as a ‘sandwich’ layer in organic solar cells and was shown to increase efficiency REF, but some discussion about the mechanism by which this improvement is achieved still exists in the literature REF.

Having established why the combination of ferroelectric polymer with silicon solar cells may be of potential societal benefit and research interest, the polymer material will be introduced in detail in the following Section. In Section 1.4 the diverse experimental methods used throughout this project are introduced from a theoretical standpoint and in Section 1.5 the experimental approach is outlined and the obtained results are reported and discussed. The concluding Section gives a short summary of this part of the project and tries to analyse its failures as well as partial successes.

---

<sup>1</sup>An added advantage of concentrators is that they allow collection of light over a great area with relatively cheap lens materials and minimise the area necessary for the costly actual cell.

## 1.2 Ferroelectricity

Ferroelectricity is best described in analogy to the more well-known phenomenon ferromagnetism. A ferromagnetic material is a material that can retain a magnetisation even when the external magnetic field is removed. Ferromagnetism lies at the heart of virtually all permanent magnets. In analogy, a ferroelectric material, is a material that can retain an electric polarisation even when the external electric field is removed. In this context “poling” is the process of giving the material a remnant polarisation. To understand polarisation, a description in terms of dipoles is illuminating. The following discussion is largely based on Atkins [5, Chapters 18.1 to 18.3 and 20.10] but is expressed in terms of macroscopic physical quantities instead of in microscopic thermodynamic quantities, e.g. susceptibility instead of polarisability. When an external electric field is applied to a material, bound charges elements are displaced: positive charge moves with the field, negative charge moves against it, setting up a dipole moment even when the material remains electrically neutral. The polarisation density  $\vec{P}$  is then defined for a certain volume element  $\Delta V$  of the material carrying a certain dipole moment  $\Delta \vec{p}$  as:

$$\vec{P} \equiv \frac{\Delta \vec{P}}{\delta V}. \quad (1.1)$$

The relationship between applied electric field  $\vec{E}$  and  $\vec{P}$  is not always easy to establish. It is therefore practical to introduce the experimentally accessible electric displacement field  $\vec{D}$ , which is defined as:

$$\vec{D} \equiv \epsilon_0 \vec{E} + \vec{P} \equiv \frac{1}{\mu_0 c^2} \vec{E} + \vec{P}, \quad (1.2)$$

with the permittivity of free space  $\epsilon_0 \approx 8.85 \cdot 10^{-12} \text{ F/m}$  which is defined by the vacuum permeability  $\mu_0$  and the speed of light  $c$  as above. In a homogeneous linear isotropic dielectric medium, the polarisation density is proportional to the electric field and related to it by its electric susceptibility  $\chi$ , a scalar quantity:

$$\vec{P} = \chi \epsilon_0 \vec{E} \quad (1.3)$$

and the susceptibility is related to the electric permittivity of the material  $\epsilon$  as:

$$\chi + 1 = \frac{\epsilon}{\epsilon_0}. \quad (1.4)$$

In anisotropic materials, it is possible that an electric field applied in one direction can lead to a polarisation in a different direction. The scalar susceptibility is therefore replaced by a susceptibility matrix which relates the  $n^{\text{th}}$  component of the polarisation to the  $m^{\text{th}}$  component of the electric field:

$$P_n = \sum_m \epsilon_0 \chi_{n,m} E_m \quad (1.5)$$

and in non-linear materials, the linear susceptibility  $\chi^{(1)}$  is expanded with second and third-order susceptibilities  $\chi^{(2)}$  and  $\chi^{(3)}$  respectively. Furthermore, because polarisation is dependent on the displacement of charges, i.e. the reorientation of dipole moments, the susceptibility is also a function of the frequency of the applied electric field. It is entirely possible to apply an electric field that oscillates so quickly that the dipoles simply do not have enough time to rearranges themselves. These effects are succinctly

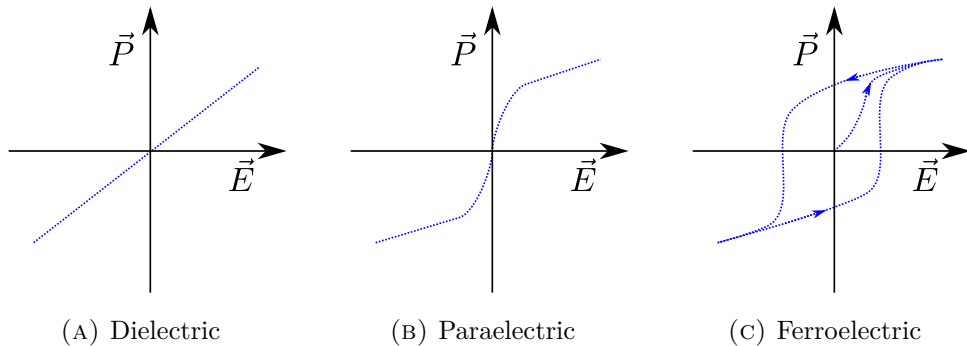


FIGURE 1.1: Schematic polarisation plots for different types of materials.

summarised in Maxwell's equations in matter, specifically in his formulation of Gauss' law. In ferroelectric materials, however, the above description usually fails, because the polarisation is not only dependent on the applied field, but also on its own history, i.e. ferroelectric materials exhibit hysteresis.

In Figure 1.1 three polarisation plots,  $\vec{P}$  vs.  $\vec{E}$ , for three different classes of materials are shown. Figure 1.1a shows the behaviour of a ‘normal’<sup>2</sup> dielectric material. The slope of the polarisation curve corresponds to the material’s electric permittivity  $\epsilon$  and is a constant. Figure 1.1b depicts the behaviour of a paraelectric material. The ‘kink’ in the curve is explained by the material becoming inherently polarised at an applied electric field: once a certain threshold applied magnetic field is reached, all previously unaligned dipoles in the material are aligned against the applied field and weaken it to the maximum extend possible for that material. When the external field is removed, the dipoles return to their unaligned state and the material thus loses its polarisation. Lastly, Figure 1.1c depicts the polarisation plot of a ferroelectric material. These materials exhibit a spontaneous electric polarisation that can be reversed by an applied field, leading to a hysteretic loop in the polarisation plot. As the applied field strength increases, so does the material’s polarisation up to a point where all dipoles are aligned against the applied field. This alignment is retained in the material, leading to a non-zero polarisation at zero applied electric field. When the field is applied in the reverse direction and reaches a sufficient strength, the ordering in the material reverses as well, leading to symmetry around the axes observed in the polarisation plot.

It is usual for a ferroelectric material to lose its ferroelectricity above a material specific Curie temperature  $T_C$ , i.e. most ferroelectric materials undergo a ferroelectric/paraelectric phase transition at  $T_C$  because the internal dipoles are coupled to the material lattice. Temperature naturally influences the lattice and therefore, the dipoles, see Figure 1.2 for an overview of the structural phases at different temperatures. Ferroelectric transitions are broadly classified into two main groups at the extremes of a continuous spectrum: order-disorder and displacive transitions [1, pp. 467 ff.]. Order-disorder transitions are relatively simply characterised by the fact that the in the unit cells point in random directions above  $T_C$ . In a displacive transition, the polarisation of the material becomes unusually large, leading to a ‘polarisation catastrophe’: the local electric field caused by a displacement of charge is stronger than the elastic restoring force, leading to an asymmetrical shift of charges. In close analogy with ferromagnetism, ferroelectric domains may exist in a ferroelectric material. Each domain is characterised by a polarisation in the same direction, whereas adjacent domains have a polarisation

<sup>2</sup>i.e. linear, homogeneous, isotropic

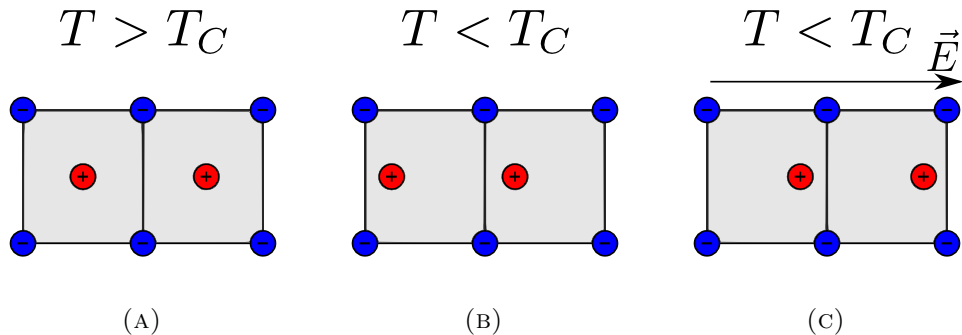


FIGURE 1.2: Schematic representation of the structural phases in a ferroelectric at a temperature above the Curie temperature (1.2a), below the Curie temperature (1.2b) and below the Curie temperature in the presence of an external electric field (1.2c). Adopted from Kittel [1, p. 478].

in a different direction. The net polarisation of the material is the vector-sum of the contributions of the individual domain polarisations and the total polarisation of the material can be changed by movement of domain walls or by nucleation of new domains.

### 1.3 Polyvinylidene Difluorite and its Copolymers

Polyvinylidene difluorite (P(VDF)) is a ferroelectric polymer that is used on an industrial scale as a speciality plastic. On the industrial level, it is largely more interesting because its chemical properties than its ferroelectricity: its melting point,  $\sim 177^\circ\text{C}$ , is relatively low compared to other fluoropolymers and is therefore more easily processed, yet it retains the stability with respect to acids, bases, solvents and heats typical for the fluorofamily. It is an insulator with a relatively low density,  $\sim 1.8\text{ g/cm}^3$ , and high mechanical strength. It is therefore often used for piping, wire-insulation, tubing etc. With regards to its ferroelectric behaviour P(VDF) is often employed as a copolymer which includes trifluoroethylene (TrFE) in its chains. These copolymers are collectively referred to as P(VDF-TrFE) usually identified by the molar ratio of their constituent difluoro- and trifluoroethylene groups. For this project P(VDF-TrFE 70:30) was available and except where otherwise specifically noted, the terms P(VDF) and P(VDF-TrFE 70:30) may be used synonymously. An approximate chemical structure for P(VDF-TrFE 70:30) is depicted in Figure 1.3. The structure is only approximate because the exact position of TrFE in the chain is random, but will on average approach a distribution that reflects the molar ratio.

The ‘*Encyclopedia of Smart Materials*’ devotes an entire Chapter to polyvinylidene

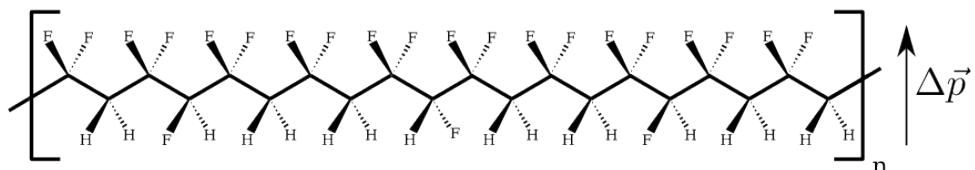


FIGURE 1.3: An approximate chemical structure for P(VDF-TrFE 70:30). The direction of the dipole moment, from Hydrogen to Fluorine, is indicated.

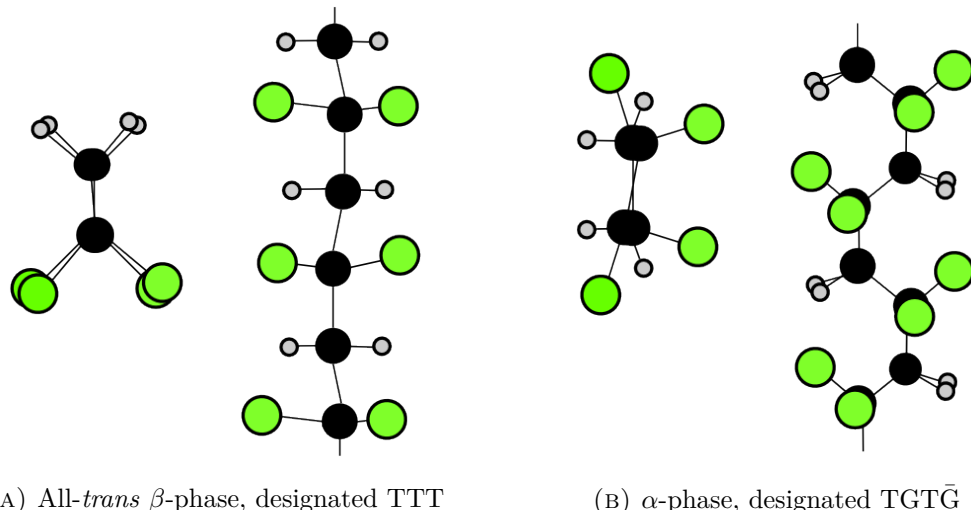


FIGURE 1.4: Along-the-chain and top down views of ball and stick models for two crystalline forms of pure P(VDF). Fluorine atoms are green, carbon black, hydrogen grey. Adopted from [2, p. 809].

difluorite and its copolymers [2, pp. 807-820] and much of the following discussion is largely based on this excellent summary.

Overall, the structure of the (co)polymer is semi-crystalline and will consist of ordered regions of monomer units, crystallites of  $\sim 10$  nm to 20 nm surrounded by a sea of amorphous, scrambled chains. The polymer may furthermore include regions of head-to-tail bonding ( $-\text{CH}_2-\text{CF}_2-\text{CH}_2-\text{CF}_2-$ ) alongside regions of tail-to-tail and/or head-to-head bonding ( $-\text{CH}_2-\text{CF}_2-\text{CF}_2-\text{CH}_2-$  and  $-\text{CF}_2-\text{CH}_2-\text{CH}_2-\text{CF}_2-$  respectively) which can be categorised as defects in the crystalline regions of P(VDF). In the case of the copolymer, TrFE is incorporated atactically into the molecule, i.e. the position of the third vinyl-group with respect to the chain <sup>3</sup> is random. Disregarding these defects, there are four major crystalline forms of P(VDF) which are described by the way the chains are packed within the crystal lattice: according to their conformations (*trans* (T) or *gauche* (G) linkages), their orientation about the chain axis (*parallel* or *antiparallel*) and the relative directions of adjacent chains (*up-up* when pointing in the same and *down-down* when pointing in opposite directions). Figure 1.4 depicts two of the the major crystalline forms and it is apparent from the Fischer-projections in Figure 1.5 that the all-*trans*  $\beta$ -phase will be preferred, resulting in a dipole-moment of  $\sim 2.1$  D <sup>4</sup> in pure P(VDF) [2, p. 810]. Figure 1.6 compares the orthorhombic unit cells of the  $\beta$ - and  $\alpha$ -phases of P(VDF) and shows an absence of a permanent dipole in the latter. The polymer chain lies along the  $\vec{c}$  unit cell vector. Table 1.1 summarises the lattice dimensions and angles of pure P(VDF) in the the  $\alpha$ - and  $\beta$ -phase and includes lattice parameters for the  $\beta$ -phase of P(VDF-TrFE) of varying molar ratio. It is apparent that introducing a third Fluorine atom into the unit cell will reduce the net dipolar moment of the monomer unit, but because of atacticity, the net dipole-moment is still parallel to the  $\vec{b}$  unit cell vector. The macroscopic effect on the net polarisation may not be as easily inferred because inclusion of TrFE may influence the superstructure of the polymer, the ordering of its crystallites and possibly

---

<sup>3</sup>Either ‘in front of’ or ‘behind’ the chain

<sup>4</sup>The debye is a CGS-unit convenient for molecular dipole-moments. It is exactly equivalent to  $1 \cdot 10^{-21}$  Cm divided by the speed of light and approximately equal to  $0.2082$  e $\text{\AA}$ .

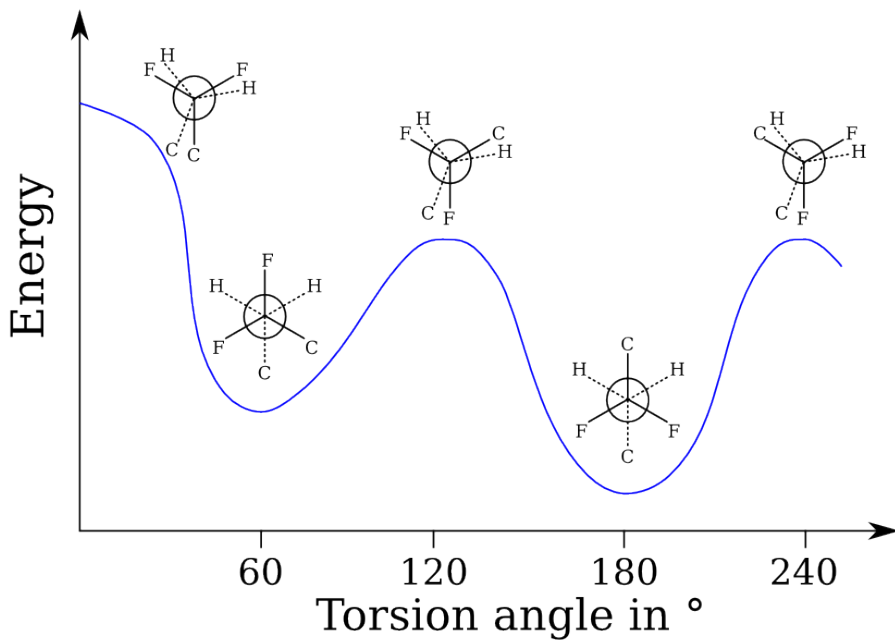


FIGURE 1.5: Fischer-Projections and internal energy as a function of the torsion angle along the chain. The minimum at  $180^\circ$  corresponds to the *trans*  $\beta$ -phase. Adopted from [2, p. 809].

TABLE 1.1: Experimental Lattice Dimensions and Angles of pure P(VDF) ( $\alpha$  and  $\beta$ ) and of P(VDF-TrFE) ( $\beta$ ) of varying molar ratio. Compiled from [2, p. 810].

| TrFE content<br>in mol% | Crystalline<br>Phase | Lattice Dimensions (Å) |      |      | Lattice Angles (°) |         |          |
|-------------------------|----------------------|------------------------|------|------|--------------------|---------|----------|
|                         |                      | a                      | b    | c    | $\alpha$           | $\beta$ | $\gamma$ |
| 0                       | $\alpha$             | 4.69                   | 9.64 | 4.62 | 90                 | 90      | 90       |
| 0                       | $\beta$              | 8.58                   | 4.91 | 2.56 | 90                 | 90      | 90       |
| 25                      | $\beta$              | 8.86                   | 4.62 | 2.56 | 90                 | 90      | 90       |
| 50                      | $\beta$              | 9.12                   | 5.25 | 2.56 | 90.3               | —       | —        |

the structure of its ferroelectric domains. The ferroelectric/paraelectric phase transition in P(VDF) is an order-disorder transition of first order [6]. The  $\delta$ -phase will not be discussed here. Because of unfavourable, repulsive van der Waals interactions introduced by the third Fluorine, the melting point of the copolymer decreases with increasing TrFE content and for the same reason, incorporating TrFE furthermore favours crystallisation into the  $\beta$ -phase. It can be seen in Figure 1.6 that the Fluorines in the  $\alpha$  unit cell are more closely packed. Therefore, melting temperature  $T_m$ , phase transition temperature  $T_C$ , degree of crystallinity, remnant polarisation  $P_r$  and coercive field  $E_C$  are all affected by the TrFE content, which is summarised in Table 1.2. However, even if the polymer is present in the ferroelectric phase, its ferroelectric domains will non the less be oriented in all crystallographically allowed directions. For an observable net polarisation to develop, the polymer therefore has to be ‘poled’: in a strong electric field, dipolar ordering will be added to crystalline ordering. Elevated annealing temperatures will help with this process even if  $T_C$  is exceeded, because as the polymer cools down, the preferred ferroelectric phase will crystallise with a higher degree of oriented ferroelectric domains. The effect

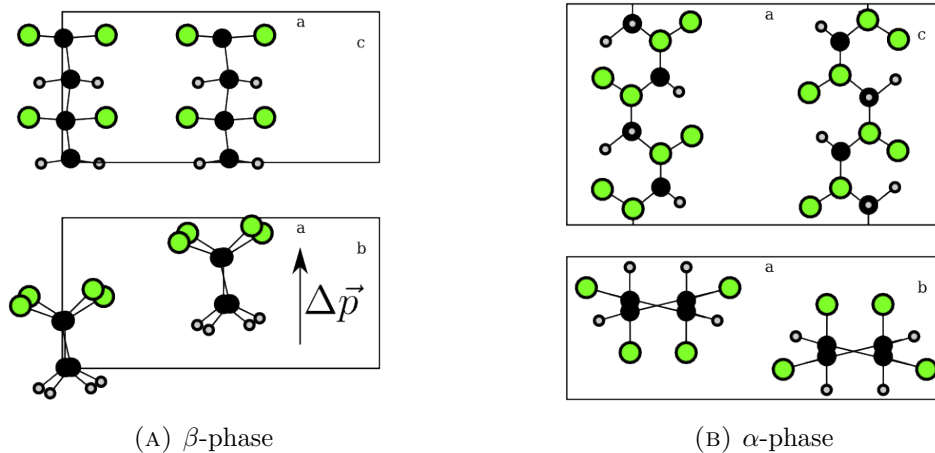


FIGURE 1.6: Schematic representations of the unit cells of two crystalline phases of P(VDF). Fluorine atoms are green, carbon black, hydrogen grey. The direction of the dipole moment in the  $\beta$ -phase is indicated. Adopted from [2, pp. 809 f.].

TABLE 1.2: Degree of crystallinity, melting temperature  $T_m$ , phase transition temperature  $T_C$ , remnant polarisation  $P_r$  and coercive field  $E_C$  for P(VDF-TrFE) copolymers of varying molar ratio. Some values are approximations because data was visually compiled from figures [2, pp. 812 f.].

| TrFE content<br>in mol% | Crystallinity (%) | $T_m$ (°C) | $T_C$ (°C) | $P_r$ (mC/m <sup>2</sup> ) | $E_C$ (MV/m) |
|-------------------------|-------------------|------------|------------|----------------------------|--------------|
| 0                       | 50                | 178        | ~195       | 50                         | 50           |
| 22                      | 80 ± 4            | 150        | 140        | ~63                        | 65           |
| 26                      | 84 ± 4            | 150        | 130        | 75                         | ~69          |
| 31                      | 88 ± 4            | 145        | 110        | ~83                        | 70           |
| 36                      | 91 ± 4            | 160        | 94         | ~93                        | 75           |
| 50                      | 73 ± 4            | ~163       | 55         | 63                         | 45           |

of annealing temperature on crystallinity and remnant polarisation for a P(VDF-TrFE) with 32 mol % TrFE is shown in Figure 1.7. Poling is usually accomplished either by electroding the polymer surfaces or by the use of a corona discharge where charge is injected into the polymer. For this project, electrode poling, both contacted and non-contacted, was attempted. Lastly, it was reported that P(VDF) thin films obtained from Langmuir-Blodgett (LB) deposition crystallise directly in the  $\beta$ -phase and undergo self-polarisation [7, 8]. However, LB deposition was not easily available during the course of this project and this route could therefore not be explored.

### 1.3.1 P(VDF) Nanoparticles

Apart from bulk material and thin films, P(VDF) can also be prepared as nanoparticles (NPs) and as nanostructured material. While interesting, P(VDF) nanostructures require sophisticated preparation steps, whereas P(VDF) NPs can easily be synthesised by a scalable, solution chemistry self-assembly mechanism which sidesteps the otherwise necessary high annealing temperatures, rendering this route especially interesting for the application with organic photovoltaic cells (OPVs). The reproducible synthesis was

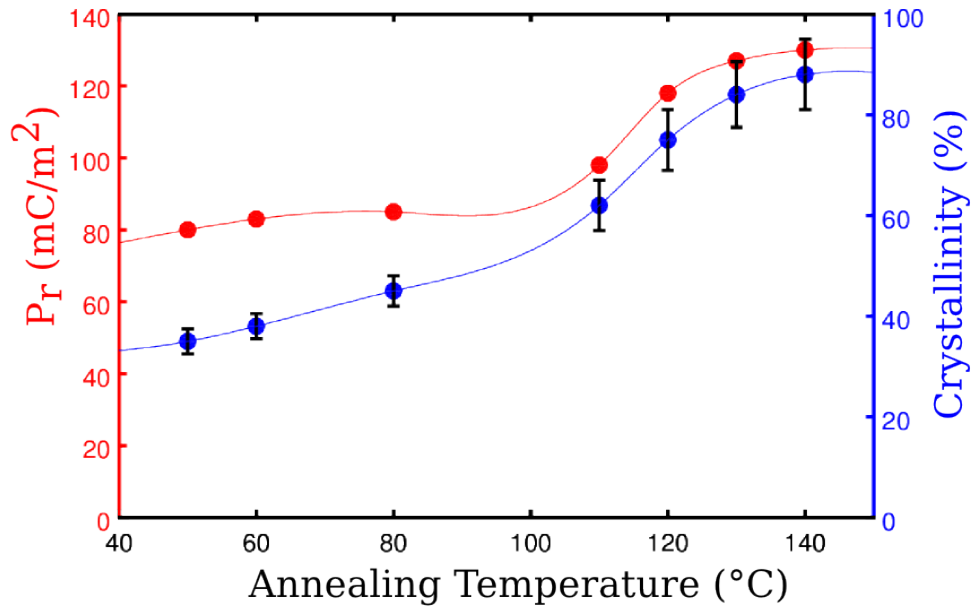


FIGURE 1.7: Effect of annealing temperature on remnant polarisation  $P_r$  and degree of crystallinity in P(VDF-TrFE) with a TrFE content of 32 mol %, adopted from [2], p. 813]. The line through the data points was constructed with a spline fit and is not based on a physical model.

first described by Xiao *et al.* [9] and their paper serves as a basis for the following discussion of the properties of P(VDF) NPs. To achieve self-assembly of P(VDF)-chains into nanoparticles, the polymer is first dissolved in a ‘good’ solvent, such as acetone, and then an interface with a ‘bad’ solvent, such as water, is formed. At the interface, P(VDF) chains tend to coils in on themselves because of the strong hydrophobic interaction between water and fluorine in P(VDF). This process is supported by precipitating the NPs out with the help of a high speed centrifuge at speeds around 20 000 rpm. Because water cannot form hydrogen bonds with the polymer [10], an increase in entropy results, causing subsequent polymer chains to aggregate at the surface of the forming NP. The NPs crystallise in P(VDF)’s amorphous, non-ferroelectric phase but can be converted to the crystalline, ferroelectrically active  $\beta$ -phase by heating above its Curie temperature. This is achieved by refluxing the suspension of NPs, which can subsequently be processed further. Spin-coating, evaporating or simply mixing the suspension with other chemicals allow for the NPs to be included in OPVs in a non-destructive, controlled manner: for example, Xiao *et al.* could independently optimise the nanoparticle size and their coverage in the solar cell. P(VDF) is a non-conducting polymer and as such increases the series resistance of the solar cell, counteracting its positive influences on charge carrier recombination lifetimes. For the optimised coverage of 18 %, the solar cell’s efficiency could be improved by 1.9 % from 4.74 % to 6.64 % which is a sizeable relative improvement of  $\sim 29 \%$ !

## 1.4 Experimental Techniques

### 1.4.1 Contact Potential Difference and Surface Photovoltage

Chapter 2 deals exclusively with the contact potential difference (CPD) and the surface photovoltage (SPV), so any theoretical or practical explanation will be skipped here. For the scope of this Chapter, it is sufficient to mention that CPD measures the work function of a sample compared to a known reference and that SPV can be an indicator of charges trapped at the surface and the overall quality of a chemical or physical surface modification. Previous work carried out at the Cahen group often focused on chemical surface modifications of silicon and it was shown for a range of chemicals that a (surface) dipole can influence the work function of the underlying silicon substrate. It is therefore assumed that successfully adsorbed P(VDF) should influence the work function of silicon as measured by CPD and that the direction of this influence be tuneable by changing the polarisation-direction of the ferroelectric polymer. It is furthermore assumed that a change in SPV may be taken as an indication of either less surface recombination or the presence of an electrical field at the surface.

### 1.4.2 Determination of Excess Carrier Lifetimes

In semiconductors, photogenerated excess charge carriers may recombine via different mechanisms. The effects of each of these mechanisms can be described by individual recombination rates,  $S$  or by individual characteristic recombination ‘lifetimes’,  $\tau$ . Generally, a distinction has to be made between recombination in the bulk as expressed by the bulk carrier lifetime  $\tau_B$  and recombination at surfaces as expressed by the surface lifetime  $\tau_S$ . These two lifetimes combine to an effective carrier lifetime  $\tau_{\text{eff}}$  given by:

$$\frac{1}{\tau_{\text{eff}}} = \frac{1}{\tau_B} + \frac{1}{\tau_S}. \quad (1.6)$$

For the bulk, three mechanism can be identified: radiative recombination (also known as band-to-band recombination),  $\tau_{\text{rad}}$ , where carriers of opposite charge neutralise each other and emit a photon of corresponding energy; Shockley-Read-Hall recombination,  $\tau_{\text{SRH}}$ , where carriers recombine via traps within the bandgap and Auger recombination,  $\tau_A$ , where opposite carriers recombine and transfer their energy to a third carrier, which subsequently gives off its excess energy in the form of heat. In the presence of these mechanisms,  $\tau_B$ , is given by:

$$\frac{1}{\tau_B} = \frac{1}{\tau_{\text{rad}}} + \frac{1}{\tau_{\text{SRH}}} + \frac{1}{\tau_A}. \quad (1.7)$$

For indirect bandgap semiconductors such as silicon,  $\tau_{\text{rad}}$  is typically large compared to the other times and may be neglected in Equation (1.7). Conversely, for (high quality) direct bandgap semiconductors such as GaAs,  $\tau_{\text{rad}}$  is short and  $\tau_{\text{SRH}}$  is typically large and may often be neglected [11]. Because Auger recombination is a three-particle process, it is inherently less probable than its two-particle counterparts. However, the Auger recombination rate is a cubic function of excess carrier density and therefore becomes dominant at higher carrier concentrations [12]. Surfaces are natural defects in the crystal structure and as such provide ample opportunity for carriers to recombine. It is more difficult to generally relate the surface recombination velocities  $S_S$  to a surface recombination lifetime which can be used in Equation (1.6). For example, the two large surfaces of a wafer might have different recombination velocities and in very high quality

semiconductors, even the comparatively small surfaces at the edges may influence the overall effective lifetime [13].

One method to measure the effective lifetime of the excess carriers of a semiconductor is to convert its photoconductance into its excess carrier density via known mobility functions:

$$\Delta n = \frac{\Delta\sigma}{qW(\mu_n\mu_p)}, \quad (1.8)$$

where  $\sigma$  is the conductance,  $\Delta n$  denotes the excess carrier density,  $W$  is the sample thickness,  $q$  the charge and  $\mu_n$  &  $\mu_p$  are the mobilities of negative and positive carriers respectively. The situation is complicated because the mobilities generally are functions of the doping densities and also of the excess carrier density [14]. Therefore, some knowledge about the sample is required and modelling the characteristics of the sample is generally applied. The carrier concentration in Equation (1.8) can be converted to lifetimes by solving the continuity equations to obtain:

$$\tau_{\text{eff}}(\Delta n) = \frac{\Delta n(t)}{G(t) - \frac{d\Delta n}{dt}}, \quad (1.9)$$

in which  $G(t)$  is the photogeneration rate and  $\Delta n$  is, again, the excess carrier density [15]. Equation (1.9) is generally valid and was even derived for non-uniform photogeneration in the presence of significant surface recombination. Most measurements are realised by flashing a strong light on the sample and monitoring the time-evolution of its photoconductance via a radio-frequency bridge. When the duration of the flash is long, a quasi-steady state situation is achieved in which the excess carrier density can be seen as constant in time. Equation (1.9) simplifies to:

$$\tau_{\text{eff}}(\Delta n) = \frac{\Delta n(t)}{G(t)}, \quad (1.10)$$

which is a good approximation for short lifetimes. A drawback of this method is that the generation rate must be known. Therefore the intensity of the flash has to be monitored, corrected for reflectivity and absorption by the sample. The opposite situation, a transient photoconductance decay measurement, is achieved then the flash is very brief and no illumination reaches the sample during the measurement. Then, the photogeneration rate can be assumed to be zero and Equation (1.9) can be solved to obtain:

$$\tau_{\text{eff}}(\Delta n) = -\frac{t}{\ln(\Delta n)}. \quad (1.11)$$

This approach is only valid for relatively long lifetimes, but the intensity of the flash does not need to be monitored and reflectivity & absorption of the sample do not need to be known, either. The combined quasi-steady-state, quasi-transient approach as described by Equation (1.9) yields the most accurate results, but is also the most involved. For this approach to work, the intensity of the flash must be measured in real-time and the absolute conductance of the sample must be known, as described by Sinton *et al.* [16, 17]. In all cases, if one is interested in the surface recombination velocities or lifetimes,  $\tau_{\text{eff}}$  needs to be translated into  $\tau_B$ . Experimentally, this can most easily be achieved by using a high quality substrate in which  $\tau_B \gg \tau_{\text{eff}}$ . If the latter is not the case, then there is an

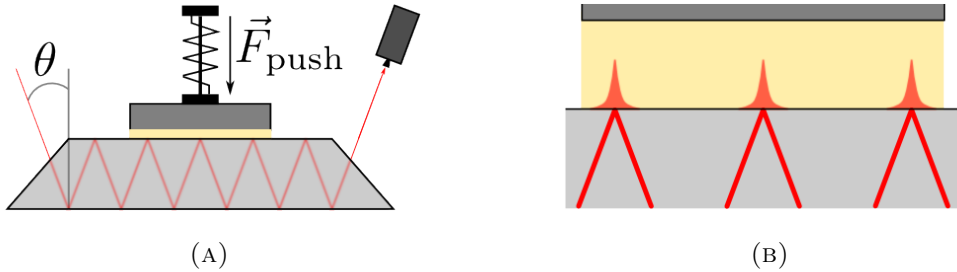


FIGURE 1.8: Schematic of an ATR FTIR set-up. Figure 1.8a shows the internal reflection of the beam of light at the edges of the guiding crystal (light gray) and the thin film sample (yellow) on its substrate (dark grey) being pressed onto the crystal. Figure 1.8b focuses on the evanescent wave projecting into the thin film and gives an indication how the beam, while being nominally inside the crystal, can still be attenuated by the sample. Adopted from VILAN.

exact equation that can be used for transient measurements:

$$S_S = \sqrt{D \left( \frac{1}{\tau_{\text{eff}}} - \frac{1}{\tau_B} \right)} \tan \left( \frac{W}{2} \sqrt{D \left( \frac{1}{\tau_{\text{eff}}} - \frac{1}{\tau_B} \right)} \right), \quad (1.12)$$

where  $D$  is the minority carrier diffusivity and the other symbols have their usual meaning [18]. A series of approximations to that equation exists and they are valid if  $\tau_{\text{eff}} \gg \frac{W^2}{\pi^2 D}$  for transient measurements and if  $\tau_{\text{eff}} \gg \frac{W^2}{12D}$  for quasi-steady state measurements [19].

### 1.4.3 Infrared Spectroscopy

Infrared (IR) spectroscopy is a vibrational spectroscopy which employs light with energies just below the visible spectrum, i.e. with wavelengths longer than  $\sim 800$  nm. It is common to express the spectrum in terms of its frequency and a typical unit is reciprocal centimeters ( $\text{cm}^{-1}$ ), also called ‘wavenumbers’ and to divide it into three broad regions: ‘near IR’ ( $\sim 14 \cdot 10^3 \text{ cm}^{-1}$  to  $4 \cdot 10^3 \text{ cm}^{-1}$ ), ‘mid IR’ ( $\sim 4 \cdot 10^3 \text{ cm}^{-1}$  to  $0.4 \cdot 10^3 \text{ cm}^{-1}$ ) and ‘far IR’ ( $\sim 400 \text{ cm}^{-1}$  to  $10 \text{ cm}^{-1}$ ), where each region approximately excites different types of vibrations ranging from harmonic to rotational-vibrational excitations. Vibrational modes are IR-active if there is a change in dipole moment which enables interaction with the electric field of the radiation. Therefore IR spectroscopy is very sensitive to the chemical environment of the sample under investigation and is especially frequently used in organic chemistry. Practically, instead of scanning each wavenumber individually, the sample is often illuminated by a wide range of radiation and decomposed by a Fourier transformation into its components, yielding Fourier Transform IR (FTIR) spectroscopy which shortens the time of the measurement and allows detecting small quantities of and minute changes in a sample.

To study thin films that are either physically or chemically adsorbed to a substrate surface, it is useful to exclude interaction of the substrate with the IR-radiation and to maximise the interactions interactions that are of interest. One method that accomplishes both these goals is Attenuated Total Reflectance (ATR) FTIR where the IR beam is directed into a crystal of high refractive index and reflects internally from its surfaces. Refer to Figure 1.8 for a schematic of the ATR method. The thin film under investigation

is pressed onto the crystal to form an intimate contact so that an evanescent IR wave can project into it, see Figure 1.8b. There, part of the IR spectrum is absorbed by the sample and the now somewhat reduced beam is returned into the crystal where it can be internally reflected to be projected into the thin film again multiple times, greatly attenuating the absorption of the thin film. As can be deduced from Figure 1.8a, the reflectance is given by

$$R(\lambda)^N = (1 - a_\lambda \cdot d_e)^N, \quad (1.13)$$

where  $N$  is the number of reflections taking place at the crystal/thin film interface <sup>5</sup>,  $a_\lambda$  is the wavelength specific absorptivity of the thin film and  $d_e$  is its effective thickness. One complication that needs to be mentioned is that ATR spectra are not linear with wavenumber CITE VILAN and therefore sometimes difficult to compare to transmittance spectra. In the context of this study, that complication is somewhat alleviated because we will mainly compare ATR-FTIR spectra relative to other other ATR-FTIR spectra to assess whether or not a phase transition has occurred in the thin film sample and will for the most part not need absolute quantification of the samples.

#### 1.4.4 Ellipsometry and Contact Profilometry

##### Ellipsometry

Generally, ellipsometry is an optical technique for investigating the dielectric properties of (layers of) thin films of material(s) on reflective surfaces. It is an indirect method insofar as that the information obtained from an ellipsometry measurement cannot directly be converted into the dielectric properties of the thin film under investigation. Therefore, the measured data must be compared to a model and the success of an ellipsometry measurement hinges on the quality of that model. In its most common form, ellipsometry measures the properties of light reflected from the surface of a sample. The set-up consists of a light source, a polariser, the sample, an analyser and a detector. Light with known, elliptical polarisation is employed, hence the name. This incident light can be decomposed into two components: the  $s$  component where the electrical field of the radiation oscillates parallel to the sample and perpendicular to the plane of incidence and the  $p$  component where the field oscillates parallel to the plane of incidence. Ellipsometry measures the complex reflectance  $\rho$  of the sample which consists of an amplitude component  $\Psi$  and a phase difference  $\Delta$  according to

$$\rho = \tan(\Psi) \exp(i\Delta). \quad (1.14)$$

The complex nature of the reflectance as measured by ellipsometry is readily apparent from the equation above. Per wavelength, one pair of  $\Psi$  &  $\Delta$  can be obtained. Therefore, to reach more optical parameters, a broad spectrum is often employed in ellipsometry. For the purposes of this study, ellipsometry was exclusively used to find the thickness of a layer of interest on a substrate of known composition and thickness.

##### Contact Profilometry

Contact profilometry is a conceptually exceedingly simple technique to study surfaces and their roughness. A small diamond tip is brought in contact with a surface and moved across a predefined path along that surface and vertical displacement of the stylus is measured accurately. Depending of the type of surface under investigation

---

<sup>5</sup>For the case of Figure 1.8  $N = 3$

displacements of 10 nm up to 1  $\mu\text{m}$  can typically be measured with a lateral resolution depending primarily on the size of the tip-apex, where resolutions of  $\sim 20$  nm are feasible. The diamond tip of a record player scanning a vinyl record and producing an audible, analogue signal is a very fitting analogy for contact profilometers in use today.

#### 1.4.5 Electron Microscopy

While a thorough explanation of the function and uses of electron microscopy is out of the scope of this paper, a brief introduction to Scanning Electron Microscopy (SEM) for the visualisation of nanometre sized objects will still be given. SEM is a type of electron microscopy in which a sample is raster-scanned with a focused beam of electrons. This focused beam causes the sample to emit several types of signals: secondary electrons emitted by atoms in the sample, backscattered electrons, x-rays and light of varying wavelength and intensity, all of which can be detected by sophisticated microscopes. The resolution of the microscope is not achieved as in an optical microscope or as in a Transmission Electron Microscope (TEM) where the focusing the beam and the wavelength are determining, but rather by a translation of the size of the raster on the sample to the size of the raster on the detector. Thus, SEM can cover up to six orders of magnitude of magnification and sample features at very different length scales can be investigated. Because the sample is subjected to a continuous beam of electrons, it needs to be conductive and grounded to get rid off excess charge. Charge accumulated on the sample can lead to unwanted interactions and artefacts in the visual reconstruction of the sample. For the purpose of this study, SEM was used to investigate the surface morphology of deposited thin films of a polymer, P(VDF), and nanoparticles synthesised from the same polymer. SEM was also used to obtain typical nanoparticle dimensions.

#### 1.4.6 IV-Curves

Current-Voltage curves (IV-curves) of a semiconductor or solar cell can reveal a lot of information about the semiconductor or cell under investigation, notwithstanding its conceptual simplicity. In a straight forward measurement, two contact are electrically connected to the sample and the current resulting from a precisely known applied voltage is measured accurately. With an appropriate illumination set-up, dark and light IV-curves can be obtained and compared. For an ideal diode, the dark current is given by the diode equation:

$$I = I_0 \left( \exp \left( \frac{qV}{nk_B T} \right) - 1 \right), \quad (1.15)$$

where  $I_0$  is the reverse saturation bias current,  $n$  is the ideality factor and the remaining symbols have their usual meaning. Under light conditions, a steady-state current is induced that shifts the IV-curve down, depending on the size of the photon-current, their spectrum and the cell's spectral response. A 'real' diode will also include parasitic resistances such as series resistance  $R_S$  and shunt resistance  $R_{SH}$  and the measured IV-curve will more closely follow a form corresponding to the equation:

$$I = I_0 \left( \exp \left( \frac{q(V + IR_S)}{nk_B T} \right) - \frac{V + IR_S}{R_{SH}} \right). \quad (1.16)$$

As can be seen from the above equation, the parasitic resistances can be obtained from the derivative of the IV-curve at its intersections with the axes and to put it more colloquially, parasitic resistances will result in the IV-curve being 'less square'

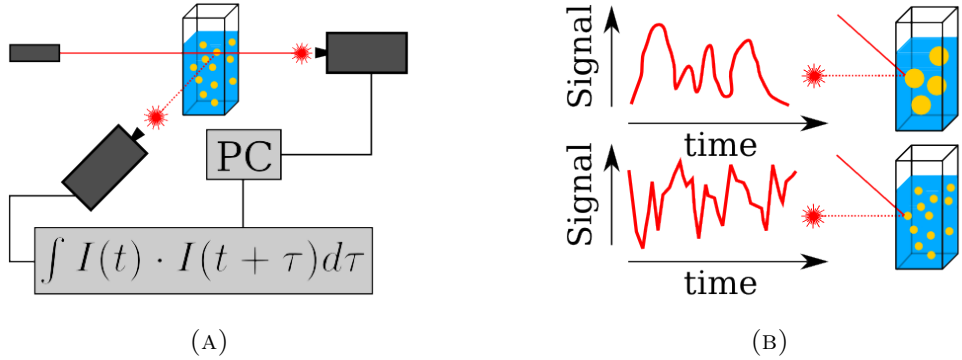


FIGURE 1.9: A schematic of a typical, simplified DLS set-up. Figure 1.9a shows the main components: (laser) source, sample cell, detectors, auto-correlator and a computer for data-sampling. Two detectors allow for measurement of relative intensity and thus help reduce unwanted noise from fluctuations in laser intensity. Figure 1.9b shows how different particle sizes lead to different ‘noise’ signatures in the measured signal.

than than of its ideal counterpart. The presence of back-diodes will result in a *S*-shaped or otherwise generally misshapen IV-curves and while it is often useful to extract precise cell parameters such as fill-factor, open-circuit voltage and short-circuit current, optical inspection of the IV-curve alone may already reveal key issues with a cell under investigation.

#### 1.4.7 Dynamic Light Scattering

Dynamic Light Scattering (DLS) is most commonly used to analyse nanoparticles, specifically it can be used to determine the size of nanoparticles in solution. The optical set-up of a DLS experiment is shown in Figure 1.9a, a typical example of the the obtained optical signal is shown in Figure 1.9b. A laser illuminates the sample, some amount of light is scattered by particles in solution and its intensity as a function of time is determined by the detector at an angle to the path of the laser beam. A second detector in the direct path of the light is used to subtract fluctuations in laser intensity. The ‘noise’ in the measured relative intensity of the two detectors is a direct consequence of the (Brownian) motion of nanoparticles in solution and will be used to extract particle size. As particles move into and out of the path of the laser, more or less light will be scattered toward the detector. Furthermore, a particle that moves about but stays within the path of the beam for a certain delay time  $\tau$  will continue to scatter light. Therefore, the evolution of the ‘noise’ in time can be understood in terms of an autocorrelation function. The mathematical treatment of the signal from a population of nanoparticles with different sizes is complicated and mathematically ill posed. To overcome this difficulty experimentally, restrictions on the size distribution have to be supplied. The following discussion will be restricted to a nanoparticle population of a single size so as not to exceed the scope of this project. For such a population, the autocorrelation function

$$C(\tau) = \sum_{t=0}^T I(t) \cdot I(t + \tau), \quad (1.17)$$

where  $T$  is the total time of the experiment,  $I(t)$  is the intensity at time  $t$  and  $I(t + \tau)$  is the intensity at time  $t + \tau$ , will also be given by a simple exponential decay:

$$C(\tau) = \exp(-2\Gamma\tau) + B, \quad (1.18)$$

where  $B$  is a baseline intensity and where  $\Gamma$  is obtained by a data-fit and is related to the (translational) diffusion coefficient  $D_t$  by the scattering vector  $q$  as:

$$\Gamma = D_t \cdot q^2 = D_t \left( \frac{4\pi n}{\lambda} \sin\left(\frac{\theta}{2}\right) \right)^2. \quad (1.19)$$

In the last equation  $n$  is the refractive index of the medium,  $\lambda$  is the wavelength of scattered light and  $\theta$  is the scattering angle. Finally,  $D_t$  as determined from the data-fit can be used in the Stokes-Einstein relation for Brownian motion to find the apparent hydrodynamic diameter  $D_h$  of the suspended particles:

$$D_h = \frac{k_B T}{3\pi\eta D_t}. \quad (1.20)$$

Here,  $k_B$  is the Boltzmann constant,  $T$  is the thermodynamic temperature and  $\eta$  is the viscosity of the suspending medium. As can easily be seen in Equation (1.20), the determined particle diameter is directly proportional to the absolute temperature  $T$ , however, the viscosity of the medium is usually also very sensitively dependent on temperature and a specific value for  $\eta$  needs to be supplied for the measurement. For practical purposes, the viscosity of typical (mixtures of) solvents in a range of temperatures is internally tabulated by software, as are their refractive indices. Therefore, the user of a DLS apparatus supplies the type of solvent used, the machine monitors the temperature during the experiment and carries out the necessary calculations and data-fitting routines. It is important to note that, for a successful size determination via DLS, a solution of nanoparticles should be sufficiently dilute to avoid clusters of nanoparticles while at the same time being concentrated enough to allow for measurable scattering intensities. Furthermore, the Stokes-Einstein relation assumes rigid, spherical particles so the apparent diameter of a soft, ovoid particle may significantly differ from its true dimensions.

The information in the presented in the preceding Section is largely based upon the presentation accompanying an advanced laboratory course taught at the Weizmann Institute of Science which is available upon request by eMail from the [author](#).

## 1.5 Experimental Approach, Results and Discussion

### 1.5.1 Sample Preparation

#### Si–H Substrates

Hydrogen passivated n-type silicon <100> with either a resistance of  $1\Omega\text{ m}$  to  $4\Omega\text{ m}$  or a resistance of  $1\text{ m}\Omega\text{ m}$  to  $5\text{ m}\Omega\text{ m}$  is prepared according to a standard procedure: pieces of suitable size are cut from a wafers with a thickness of  $\sim 300\text{ }\mu\text{m}$  and  $500\text{ }\mu\text{m}$  with a diamond tip cutter, swiped off with ethyl-acetate to remove residual dust from cutting and successively sonicated for three minutes each in ethyl-acetate, acetone, methanol and water to remove organic and inorganic contaminants. Between each successive sonication step, the pieces are rinsed off with the ‘new’ solvent to avoid solvent cross-contamination. The pieces are microwave-treated in a plasma at  $100\text{ W}$  with a flow of  $1\text{ cm}^3/\text{min O}_2$  and

1.5 cm<sup>3</sup>/min Ar for 3 minutes. This treatment oxidises the silicon and carbonises possible organic contaminants. Subsequently, samples are rinsed with pure water (18 MΩ cm at 20 °C) to remove residual contaminants and then immersed in 2 % HF etching solution for 1 minute. The strong acid removes the oxide and creates hydrophobic Si–H surface, which is rinsed with water to remove residual acid. The microwave treatment is repeated, the sample is rinsed again, etched again in HF and subsequently rinsed shortly to avoid possible oxidation by water. All chemicals are 99.9 % purity or higher. During this process, the pieces are handled with clean plastic tweezers that underwent the same sonication steps prior to experimentation. To avoid contamination, one set of tweezers is set aside for exclusive use with HF. To avoid oxidation by air, samples are either directly further processed or stored in the inert atmosphere of a glovebox (< 5 ppm O<sub>2</sub> & H<sub>2</sub>O). The procedure is practised until the surface layer thickness as determined by ellipsometry is reproducibly thinner than 10 Å and carrier lifetimes in high purity floatzone Si are measured at different stages during the cleaning procedure.

Hydrogen passivated n-type silicon <111> with a resistance of 72 Ω m to 88 Ω m is prepared according to a similar procedure: the etch in HF is replaced by either a buffered-oxide-etch (BOE) or by treatment with ammonium fluoride, NH<sub>4</sub>F.

### P(VDF-TrFE 70:30) Thin Films

P(VDF) thin films are spin-cast on Si–H from solutions of different organic solvents at different concentrations ranging from 1 mg/ml to 5 mg/ml to investigate the influence of the solvent on thin film morphology and to allow for control over the thin film thickness. Acetone, oxygen-free dimethylformamide (DMF), water-free tetrahydrofuran (THF) and cyclohexanone are used as solvents. Unless otherwise noted, 100 µl of P(VDF) solution is pipetted onto freshly prepared Si–H and spun for 5 s at 500 rpm to distribute the solution evenly and then spun for 40 s at 4000 rpm to achieve a thin film the thickness of which is determined from ellipsometry and profilometry.

The samples were annealed on a hotplate for different times ranging from 30 min to ‘over night’ at temperatures ranging from 120 °C to 140 °C. The samples were either heated gradually from room temperature to anneal temperature or placed on a preheated hotplate, because it was found that rapid thermal annealing may favour crystallisation of the β-phase [20]. Similarly, samples were either allowed to cool gradually or thermally quenched by placing on a metal plate in an ice-bath. Poling was attempted with two different set-ups at different terminal voltages ranging from 18 V to 900 V for different times ranging from 30 min to ‘over night’ at temperatures between room temperature and annealing temperature.

Poling was attempted with two set-ups one in which the P(VDF) surface is directly contacted and one in which poling is contact-less. In the former, two series-connected 9 V batteries are the voltage source. The bottom electrode is a conductive piece of copper which is connected by a screw to the source. The top electrode is a microscopy slide which is coated with a flat layer of aluminium by thermal evaporation on one side. It is contacted to the source by a strip of conductive adhesive tape. The backside of the sample is scratched, InGa eutectic is applied and the sample is firmly placed on the bottom electrode. The top electrode is placed directly onto the P(VDF) surface and weighed down with a suitable piece of metal. Neglecting possible voltage drops in the contacts, the electrodes and the silicon substrate, this set up should develop a field of  $\sim 1.8 \cdot 10^7$  V/m to  $1.8 \cdot 10^8$  V/m in the polymer layer for a polymer thickness between 100 nm to 10 nm respectively, close to or well above the coercive field strength of P(VDF-TrFE 70:30). Simultaneous annealing and poling could be achieved, but care had

to be taken to avoid burning the delicate cables. The contact-less poling device employed a high-voltage source. The bottom electrode was the same piece of copper, placed on a thick plastic insulator with a 20 cm long vertical rod attached to it. Attached to the rod, movable along it, was a piece of insulator that had a 15 cm by 15 cm aluminium plate attached to it. The source was connected to the plate via an inlet for a conductive screw in the insulating holder. The surface of the aluminium could not be assumed to be flat and would therefore not serve as a top electrode directly. Thus, a silicon wafer of low resistivity was coated with a flat layer of aluminium by thermal evaporation and was connected to the metal plate with conductive paste. The top electrode assembly was lowered above the sample and the high voltage source was turned up to a value just below the electrical breakdown of air. In this manner, an electric field strength of just below  $\sim 3 \cdot 10^6$  V/m could realistically be achieved in the polymer layer. This is about one order of magnitude lower than the coercive field of P(VDF-TrFE 70:30). However, even such a ‘low’ electric field should induce an observable polarisation by nucleation of ferroelectric domains in P(VDF) [2, pp. 812 ff.]. Specifically, Ducharme *et al.* [21] found that nucleation processes can take place in films with a thickness  $> 15$  nm and that the coercive field falls dramatically with increased temperatures. When the phase transition temperature is exceeded during annealing and recrystallisation in the  $\beta$ -phase takes place inside the electric field, dipole-ordering is energetically preferred at least to some extend. The P(VDF) thin films are characterised by relative CPD & SPV, by FTIR, by the carrier lifetimes in their substrate and their morphology is investigated by SEM. In the majority of experiments, the samples are introduced into the antechamber of a glovebox immediate after spinning to avoid oxidation and left there under reduced pressure for at least 10 min after which the antechamber was consecutively evacuated and refilled with pure N<sub>2</sub> three times to avoid contamination of the inert atmosphere. There was concern because oxygen-levels in the glovebox reached high values, so some of the experiments were carried out in ambient atmosphere until it became clear that the solvents and procedures of this project were not the cause of the contamination in the glovebox. The initial experiments with the high-voltage poling apparatus were carried out in ambient until a sufficiently empty glovebox was found to accommodate the bulk of the apparatus.

### P(VDF-TrFE 70:30) Nanoparticles

The synthesis of P(VDF-TrFE 70:30) nanoparticles follows the procedure described by Xiao *et al.* [9]. P(VDF-TrFE 70:30) is dissolved in acetone, a good solvent for the polymer, at a concentration of 5 mg/ml and a mixture of water and methanol of 1:10 by volume is prepared. These solutions and pure acetone are placed in ice and the solutions are allowed to cool down for five minutes. 2 ml of the P(VDF-TrFE 70:30)-acetone solution are injected into a 15 ml centrifuge tube. 0.5 ml of pure acetone are carefully injected from the bottom to form a buffer layer and subsequently 4 ml of the water:methanol blend are also carefully injected from the bottom. The centrifuge tube is handled carefully so as not to disturb the sensitive layers and placed in ice. The nanoparticles are then precipitated out by centrifuging at 19 500 rpm for ten minutes at 2 °C. The bottom layer containing NPs is transferred to a flask via a micro porous filter and refluxed at 90 °C for 60 min. The obtained solution contains P(VDF-TrFE 70:30) NPs and can be used for further experiments.

It was found that the time needed to transfer the prepared layers to the centrifuge should be minimised in order to obtain the smallest nanoparticle sizes from the synthesis.

Ultra-high centrifuge speeds were found to impact the narrowness of the size distribution to a small extend. Centrifuging at 16 000 rpm was still sufficient to obtain a population with a sufficiently narrow distribution.

The synthesis was carried out toward the end of the project and the problem with it became apparent too late to order a different polymer preparation: the ratio of polymer to co-polymer available for this project was 70:30 and therefore, its Curie-temperature is above the boiling point of any water:methanol mixture and indeed the synthesis by Xiao *et al.* makes use of a 50:50 polymer:co-polymer mixture. ‘Refluxing’ under conditions of increased pressure proved fruitless and substituting the water:methanol mixture with pure water in an attempt to boil under pressure at elevated temperatures was not feasible experimentally, because acetone would mix with pure water and no stable interface layers would form. Therefore, even though NPs could be synthesised, the material did not crystallise in its ferroelectric phase and the NPs could not usefully combined with solar cells. Possible further experimentation should use the appropriate polymer:copolymer mixture.

### 1.5.2 CPD SPV

#### Standard Experiments

##### Pole-Reverse-Pole

#### 1.5.3 Lifetimes

#### 1.5.4 Ellipsometry

#### 1.5.5 IR

#### 1.5.6 IV

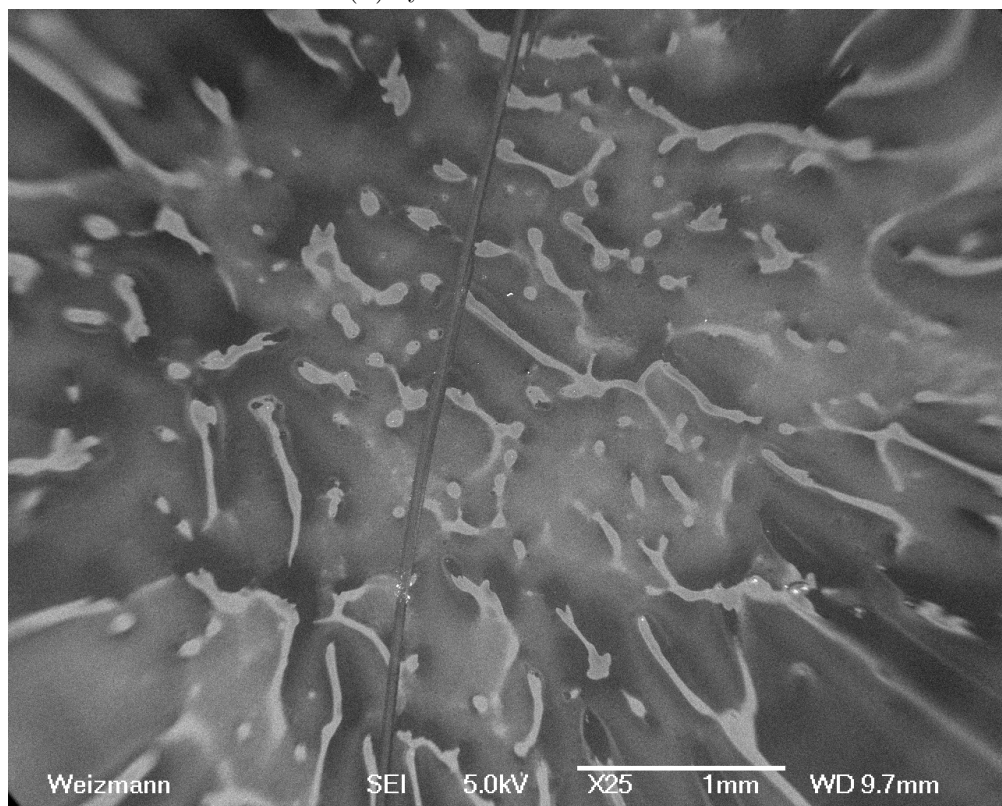
#### 1.5.7 Scanning Electron Microscopy

#### Influence of Solvent on Thin Film Morphology

Thin films were spin cast on cleaned indium tin oxide (ITO) from 5 mg/ml P(VDF) in cyclohexanone and from 3 mg/ml P(VDF) in DMF, compared in Figure 1.10. Samples were annealed at 135 °C for 30 min and the P(VDF) was carefully scratched in some places to assure presence of polymer under the SEM. The substrate was placed inside a holder which electrically contacts both the substrate backside as well as the exposed P(VDF) front surface and were introduced into a Field Emission SEM manufactured by JEOL, model JSF-7000F connected to and operated by the manufacturer’s specific software. The acceleration voltage was 5 kV and the magnification was 25-times. The film morphology obtained from cyclohexanone, Figure 1.10a is very homogeneous. The more conductive ITO surface appears darker in the image and serves as proof that polymer is indeed present in the image. Apart from the scratch, the coverage is complete. The individual bright spots are interpreted as dust particles from unusually long exposure to ambient. The scale-bar is invisible against the background of the sample, but is the same as in Figure 1.10b, as evidenced from the microscope’s log-files. DMF leads to rough, uneven P(VDF) layers with speckles and folds, as can clearly be seen in Figure 1.10b. The observations made here are in accordance with the literature [22].



(A) cyclohexanone solution



(B) DMF solution

FIGURE 1.10: SEM images comparing the P(VDF) thin film morphologies obtained from spin casting of different solutions.

TABLE 1.3: Nanoparticle diameters as obtained by SEM. Values for Xiao *et al.* are estimated from [9, Figure 1f)]. Batches b<sub>1</sub> through b<sub>3</sub> were refluxed before size determination, batches b<sub>1</sub> & b<sub>2</sub> were centrifuged at 16 500 rpm, b<sub>3</sub> & b<sub>4</sub> at 18 000 rpm.

| Batch designation  | Xiao <i>et al.</i> | NP diameter (nm) |                |                |                |
|--------------------|--------------------|------------------|----------------|----------------|----------------|
|                    |                    | b <sub>1</sub>   | b <sub>2</sub> | b <sub>3</sub> | b <sub>4</sub> |
|                    | 290                | 174              | 188            | 133            |                |
|                    | 263                | 155              | 129            | 166            |                |
|                    | 198                | 147              | 167            | 145            |                |
|                    | 283                | 153              | 124            | 148            |                |
|                    | 382                | 229              | 152            | 164            |                |
|                    | 270                |                  | 185            |                |                |
|                    | 198                |                  |                |                |                |
| Mean               | 75                 | 270              | 172            | 157            | 151            |
| Standard Deviation | 12                 | 63               | 34             | 27             | 14             |

### Nanoparticle characterisation

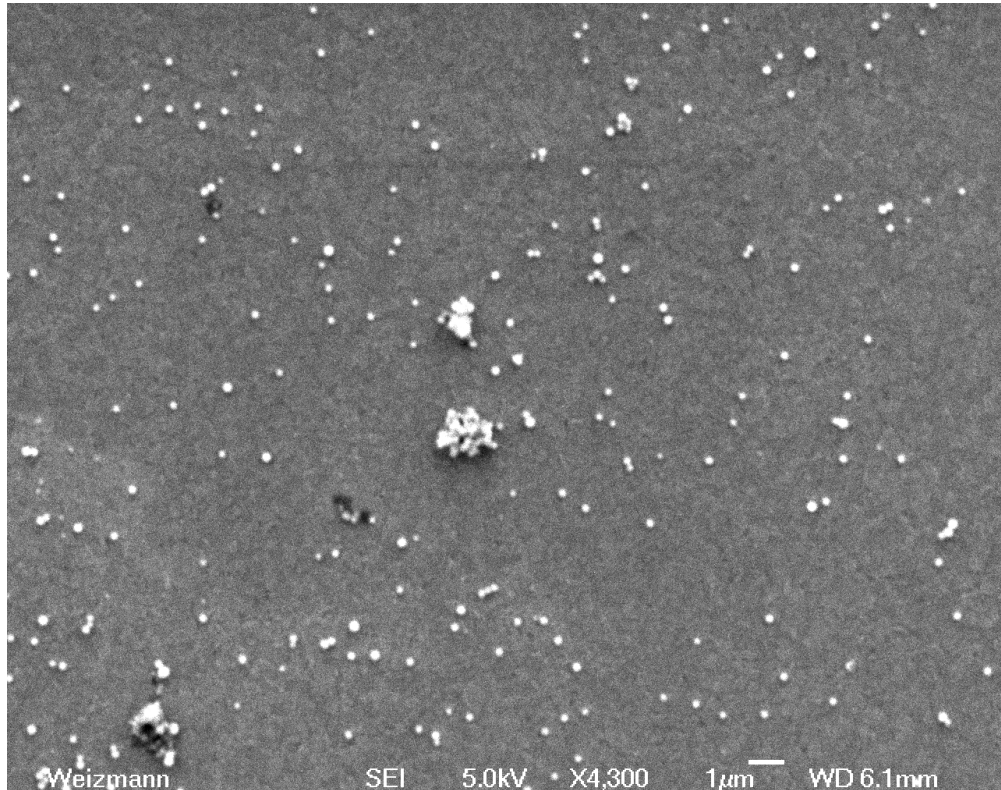
Nanoparticle suspension was pipetted onto a cleaned ITO surface and the solvent was either allowed to evaporate naturally or in one case the sample was heated to annealing temperature (135 °C). The ITO substrates were introduced into the SEM in the same manner as the thin film samples. SEM was mainly used as a tool to determine the diameter of synthesised NPs. In total 23 individual NPs from four individual batches of synthesis were measured. The very first batch was discarded because the ‘nano’ particles had an average size of ~0.9 µm. This was because instead of directly precipitating by centrifuge, the layered solutions were left standing in the lab for ~10 min. The results of the measurements of the subsequent batches are given in Table 1.3. It is interesting to note that both the average size as well as the variation in the population decrease with increasing experimental experience <sup>6</sup>. This is mainly due to faster processing of the individual synthesis steps and because later syntheses were carried out closer to the centrifuge to minimise the time the layers stay in contact without being centrifuged. The particles are about twice as big as those obtained by Xiao *et al.* [9], however, it is not immediately apparent from their paper if they used NP radius or NP diameter as a measure of size. It is assumed that diameter was used, just as in this project. Their population size distribution is narrower: standard deviation ~12 nm compared to 14 nm in this project’s ‘best’ synthesis. This may be because the centrifuging speeds for this project were instrumentally limited to 18 000 rpm instead of the prescribed 20 000 rpm or maybe because they measured 71 individual NPs instead of the five individual NPs in batch b<sub>4</sub>. SEM was also used to try to establish the overall morphology of the NPs, see Figure 1.11 for an overview of encountered structures. Figure 1.11a shows a typical SEM image of the NPs synthesised in this project. Overall, they are roughly spherical, evenly distributed and show only few clusters. Some other SEM images did not show clusters at all. Lastly, it was mentioned that the NP dispersion could not be refluxed at a sufficiently high temperature to obtain the correct crystallographic phase. It was therefore attempted to ‘anneal’ the NPs after being spun cast onto a substrate. The

<sup>6</sup>The batches are numbered as successive syntheses, i.e. b<sub>1</sub> was the first (not discarded) synthesis, b<sub>4</sub> the last that was investigated with SEM

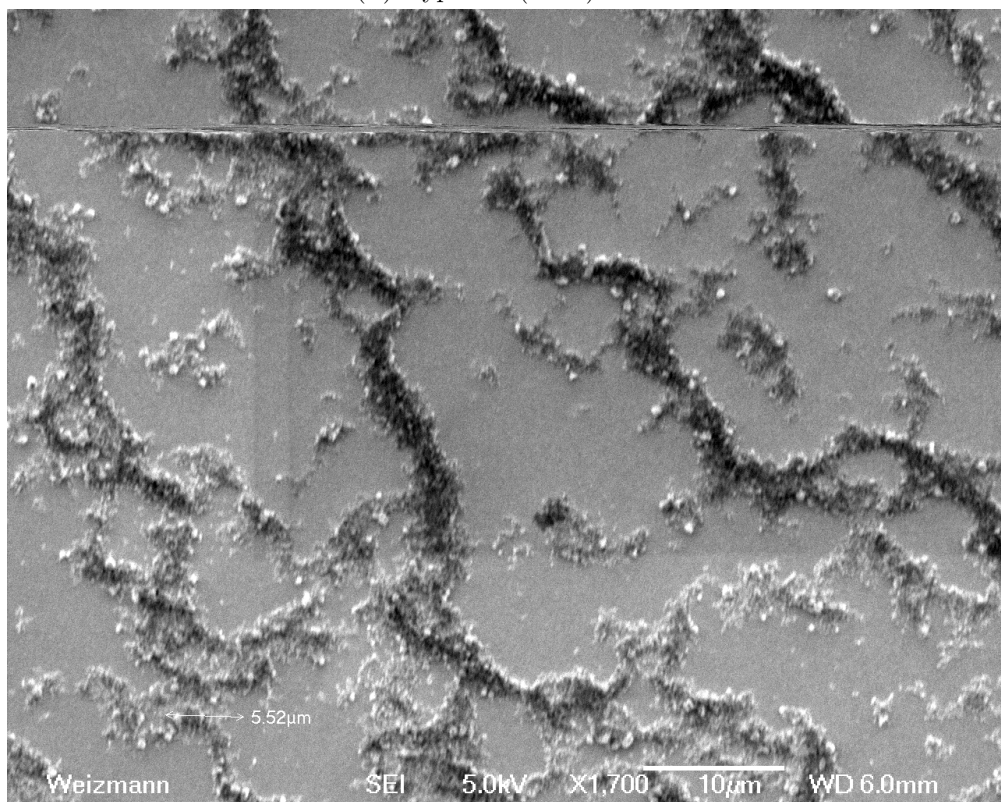
result is seen in Figure 1.11b: unsurprisingly, the NPs melted and formed amorphous structures on the substrate.

### 1.5.8 DLS

## 1.6 Discussion



(A) Typical P(VDF) NPs



(B) Amorphous structures after annealing on the substrate.

FIGURE 1.11: SEM images comparing ‘normal’ P(VDF) NPs to those that were annealed at  $T_C$  on a substrate.

## Chapter 2

# Temperature Dependent Surface Photovoltage

## 2.1 Introduction

This Chapter deals with realising and validating an experimental set-up to measure the temperature dependent surface photovoltaic (SPV(T)) with the help of a cryogenic system, a modified Kelvin probe (KP) and a suitable source of illumination. Section 2.2 will introduce the necessary physical background underlying the measurements with a KP and will be followed by a more thorough description of the actual Kelvin probes in use in Section 2.3, subdivided into a description of the already established systems (Section 2.3.1) and the ‘new’ system (Section 2.3.2). The experimental approach described in the following Sections is aimed at validating, step-by-step that the ‘new’ system reproduces results obtained with the established systems and to investigate possible complications that the capabilities of the ‘new’ system might bring to light. The experimental approach will culminate in a report of a temperature dependent measurement of the SPV for a chosen model system in Section 2.7.1. While results obtained in that last Section cannot be fully explained at this point, the measurement did serve as a useful proof of principle to show that reproducible SPV(T) measurement are feasible with the system. A brief conclusion will round off this Chapter.

## 2.2 Theory

### 2.2.1 The Contact Potential Difference and the Kelvin Probe

When two (semi-)conductors with dissimilar Fermi levels are electrically connected from their back-side with a gap between them, charge will flow from the material with the lower work function (WF) to the one with the higher WF. The work function is defined as the energy needed to remove an electron from a solid to a point in vacuum immediately outside of it. Electrons will stop flowing when equilibrium is established. As long as there is a gap between the materials, an electrical field will develop in the gap due to the difference in the local vacuum level across this gap. The potential drop across the gap, the contact potential difference or CPD. When the work functions are expressed in Electron-Volts, the CPD is directly equal to the difference of the WFs:

$$\text{CPD} \equiv \varphi_{\text{Probe}} - \varphi_{\text{Sample}}. \quad (2.1)$$

The order of the operands in the equation above is a matter of convention. Their physical representation depends on how the measurement system which we will investigate in the following – the Kelvin Probe – is set up electrically. In the configuration outline above, the materials behave like a parallel plate capacitor and a capacitance is established, which is known to be:

$$C(t) = \frac{\epsilon \epsilon_0 A}{d(t)} \quad (2.2)$$

in which  $\epsilon$  &  $\epsilon_0$  are the permittivity and the permittivity of free-space respectively,  $A$  is the area of the parallel plate and  $d(t)$  is the distance between the plates.  $d(t)$  is taken as a function of time, because the Kelvin Probe varies the distance in time. The current between the plates is given by the change in charge on the plates, which is in turn given by the change in capacitance:

$$I(t) = \frac{dQ}{dT} = \Delta V \frac{dC}{dV}, \quad (2.3)$$

where  $\Delta V$  is the difference in potential between the plates, which is the sum of the applied backing voltage and the naturally occurring potential difference between the plates, the CPD:  $\Delta V = V_{\text{Backing}} + \text{CPD}$ . If we assume a sinusoidally varying distance with the average distance between the plates being  $d_0$ ,  $d_1$  being the amplitude of oscillation,  $\omega$  being its frequency of oscillation and an arbitrary phase  $\psi$ , then

$$d(t) = d_0 + d_1 \sin(\omega t + \psi) \quad (2.4)$$

and finally

$$I(t, \Delta V) = -\epsilon\epsilon_0 A \Delta V \frac{d_1 \omega \cos(\omega t + \psi)}{(d_0 + d_1 \sin(\omega t + \psi))^2}. \quad (2.5)$$

In equation (2.5), the current is written as a function of time and potential difference between the plates, because while continuously varying the distance between probe and sample, the Kelvin Probe also varies  $V_{\text{Backing}}$ . As can easily be seen from equation (2.5), the current is zero or 'nulled' when  $V_{\text{Backing}} = -\text{CPD}$ . Thus, if  $\varphi_{\text{Probe}}$  is known,  $\varphi_{\text{Sample}}$  can easily be calculated from equation (2.1). In practice, this requires calibrating the probe head against a sample with known work function, HOPG in the context of this study. Obviously, if one wants to study the work function of a sample as a function of temperature, the temperature dependence of the work function of the probe also has to be known. In most cases and especially for simple metals, the work function only varies over a few hundredths to a few tenths of meVs per Kelvin [23, 24, 25, 26, 27]. These variations are negligible compared to other sources of experimental uncertainty and the work function of the probe is therefore assumed to be constant with respect to temperature throughout this work.

As pointed out, the work function WF of a semiconductor is defined as the energy needed to remove an electron from the material to a point in vacuum just outside of it and is given by the difference of the near surface vacuum energy  $E_{\text{vac}}$  and the Fermi energy  $E_f$  of the material:  $\varphi = E_{\text{vac}} - E_f$ . The Fermi level of a doped semiconductor is dependent on the temperature and the carrier-concentrations of the semiconductor and can be expressed in terms of the intrinsic Fermi energy as:

$$E_{f,n} = E_i - kT \ln \frac{n}{n_i} \quad (2.6) \quad \text{and} \quad E_{f,p} = E_i + kT \ln \frac{p}{p_i} \quad (2.7)$$

for n- and p-type semiconductors respectively. As can be seen from the preceding equations,  $E_f$  changes with the Boltzmann Temperature. At 300 K<sup>1</sup> and at 100 K,  $kT$  is approximately equal to 26 and 8.6 meV, respectively. In many cases, it is assumed that the extrinsic carrier concentrations  $n$  and  $p$  are equal to the product of dopant concentration and number of supplied free carriers per dopant atom. But even in that case, the concentration of intrinsic carriers is still a strong function of temperature and requires knowledge of several material parameters to calculate precisely. A simpler argument that is valid for moderately doped semiconductors in which the Fermi-Dirac distribution can be approximated by the Boltzmann distribution is developed in the following for the example of an n-type semiconductor. In such a semiconductor, the chance of finding an electron close to the conduction band edge is greater than finding a hole close to the valence band edge. Therefore, the Fermi level is closer to the conduction band. At absolute zero, all levels below the Fermi level are filled and all levels above the Fermi level are empty, by definition. At absolute zero, there can be no free electrons as freedom to move would imply energy. Therefore, at absolute zero, the Fermi level

---

<sup>1</sup>approximately room temperature

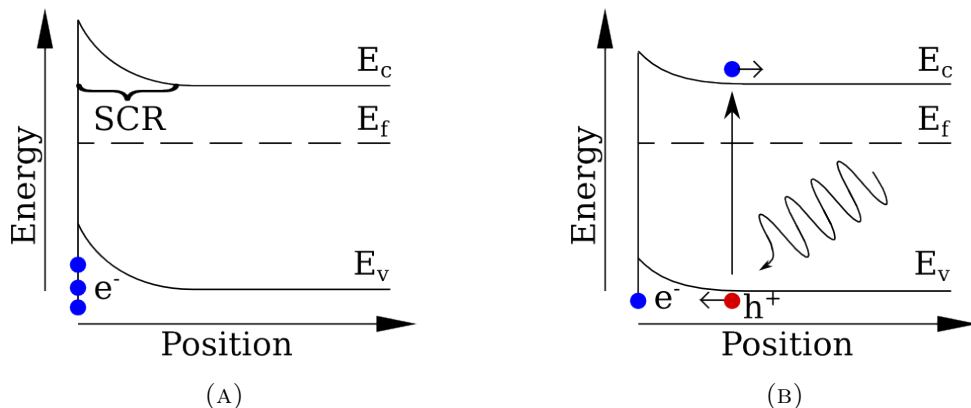


**FIGURE 2.1:** Band bending, trapped surface charges and the space charge region at the surface of an n-type semiconductor (a) in the dark and (b) under illumination. Note the decrease in trapped surface charges in (b) and the resulting reduction in band bending. Energy levels of the valence band,  $E_v$ , the Fermi level,  $E_f$ , and the conduction band,  $E_c$ , are included for reference.

cannot be above the conduction band edge. So far, it is shown that the Fermi level must be closer to the conduction band, but below its band edge. At extremely high temperatures, doping will be negligible because thermally generated carriers will exceed carriers introduced by the dopant. Therefore, the Fermi level will tend toward the intrinsic Fermi level in mid gap. A similar argument holds for the Fermi level of a moderately doped p-type semiconductor and it is therefore shown that:

$$\frac{dE_{f,n}}{dT} < 0 \quad (2.8) \quad \text{and} \quad \frac{dE_{f,p}}{dT} > 0 \quad (2.9)$$

for the Fermi level of an n-type and a p-type semiconductor, respectively.

### 2.2.2 The Surface Photovoltage and Band Bending

In the context of this work, the surface photovoltage (SPV) is defined as the CPD measured under illumination minus the CPD in the dark:

$$SPV \equiv \text{CPD}_{\text{light}} - \text{CPD}_{\text{dark}}. \quad (2.10)$$

It is instructive to refer to the diagrams in Figure 2.1 to understand the origin of the surface photovoltaic effect: in the dark, majority carriers are trapped at the surface, setting up a space charge region (SRC). For n-type semiconductors, electrons are in the majority, accumulating negative charge on the surface, setting up an electrical field pointing from the bulk toward the surface. This field causes the potential energy of electrons to be higher at the surface than in the bulk and accordingly, the bands in Figure 2.1a are bent 'up'. Of course, the situation is reversed for p-type semiconductors. Under illumination, electron-hole pairs are created where radiation of sufficient energy is absorbed. For direct band-gap semiconductors, the absorption depth is shallow and electron-hole pair generation might well occur within the SRC. For indirect band-gap materials, absorption might occur deep within the bulk and carriers might have to diffuse through the material until they reach the SRC. Regardless of their path, once the carriers are close to or within the SRC the direction of the electrical field present there causes minority carriers

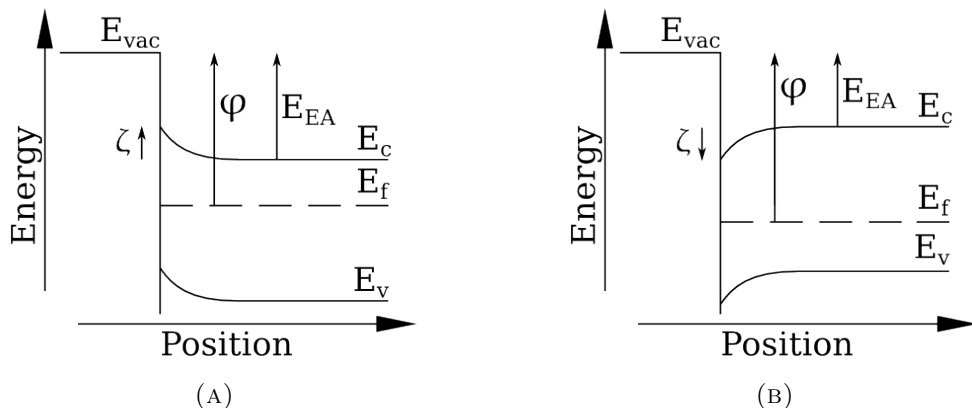


FIGURE 2.2: Definition of terms electron affinity,  $E_{EA}$ , band-bending  $\zeta$ , conduction band edge,  $E_c$ , Fermi level,  $E_f$  and work function,  $\varphi$ , for an n-type semiconductor (a) and a p-type semiconductor (b). It can be clearly seen that the band bending is negative for the p-type semiconductor. Valence band edge,  $E_v$ , included for reference.

to be attracted to the surface and majority carriers to be repulsed back to the bulk. Once the minority carriers reach the surface, they will recombine with majority carriers already present there. This causes the charge at the surface to decrease and the bands to flatten, see Figure 2.1b. When the trapped surface charge is completely neutralised, the bands will return to their initial flat state, the SRC will vanish and it is said that the SPV has saturated [28]. Saturation is usually assumed in an experiment when a further increase in illumination intensity does not lead to a further change in observed light CPD. For this reason, SPV is often the method of choice when investigating the band bending [29, 30] but it should be noted that in the presence of strong Fermi level pinning, bands might still be bent, even if SPV saturation is reached [31]. In that case, bending is not exclusively due to trapped charges and care should be taken when analysing results obtained by SPV. In a metal, the Fermi level lies within the conduction band. Therefore, carriers are free to move to and from the surface and no notable SRC will exist in a metal. Therefore, no difference in CPD between the dark and the illuminated condition is expected for a metal, so equations (2.1) and (2.10) combine to give the SPV as a function exclusively in terms of the sample material:

$$SPV = \varphi_{\text{s,dark}} - \varphi_{\text{s,light}} : \quad (2.11)$$

To gain a deeper insight into the behaviour of a semiconductor as it reacts to light, its work function can be redefined in more practical terms, namely in terms of electron affinity, band-bending, conduction band edge and Fermi level, which are shown in Figure 2.2. Here, electron affinity is defined as the energy obtained by moving an electron from vacuum just outside the semiconductor to the bottom of the conduction band edge deep inside the semiconductor, which is subtly different from its usual definitions in Chemistry

and Solid State Physics <sup>2</sup>. We have:

$$E_{EA} \equiv E_{\text{vac}} - E_c. \quad (2.12)$$

Band-bending,  $\zeta$ , is the difference in energy of the conduction band close to the semiconductor surface and deep within the semiconductor, so the work function can be given by

$$\varphi = E_{EA} + E_c - \zeta - E_f. \quad (2.13)$$

In the equation above,  $E_{EA}$  and  $E_c$  are not affected by illumination, band-banding vanishes under saturation <sup>3</sup> and  $E_f$  can change because of its dependence on the carrier concentrations as expressed in equations (2.6) and (2.7). However, if its change due to illumination is for the moment assumed to be small compared to the band bending, then combining equations (2.13) and (2.11) yields an interesting property of the SPV: its sign can be used to identify if a sample is n- or p-type. For an n-type semiconductor,  $\zeta$  is positive and thus its SPV is also a positive quantity; for a p-type semiconductor, the situation is reversed: both  $\zeta$  and SPV are negative.

## 2.3 Kelvin Probes in use

### 2.3.1 Established Kelvin Probe System

As mentioned, it was the aim of this project to establish if a combination of a cryogenic system fitted with a custom KP probe head could be used for temperate dependent measurements of the SPV. The system in question will be described in detail in Section 2.3.2, here, the focus will be on a brief description of the two Kelvin probe system that were already established and had been in use in the Cahen group for some time.

Both systems feature KP probe heads model ‘Kelvin Probe S’, manufactured by Besocke Delta Phi GmbH [32], electrical and mechanical control is provided by systems provided by the same manufacturer. Housing and illumination for the Kelvin probe set-ups are provided by in-house built solutions. The probe head consists of a 2.5 mm diameter opaque gold grid and as such provides a stable and inert reference surface for measurements of the CPD. In practice, however, the probe heads still need to be calibrated with HOPG if absolute measurements of the WF are desired because changes in humidity, contamination or other, unknown factors can greatly influence the work function of the probe heads.

The first Kelvin probe system is situated in a shielding Faraday cage placed inside a humidity controlled room (20% relative humidity) and the probe head is exposed to ambient. This system will be referred to as the ‘Ambient Probe Station’. The sample is mounted onto a conductive block of metal which is slid into a holder that provides an electrical ground for the sample specimen. Samples are either connected with InGa eutectic via their backside or with the help of an electrically conductive clip-holder screwed to the conductive block of metal. The sample is stationary and the probe head is positioned close to the surface under investigation with the help of micrometer screw gauges. Illumination of the sample is achieved with a xenon-lamp driven by a VariAC-power source with up to 60 W electrical power and an optical lens focusing

---

<sup>2</sup>In Solid State Physics  $E_{EA}$  is usually defined as the energy gained by moving an electron from vacuum just outside the material to the conduction band close to the surface, because this quantity is experimentally accessible. Our definition gives access to the band-bending,  $\zeta$ , as an independent parameter.

<sup>3</sup>in the absence of Fermi level pinning

the light onto the surface of the mounted sample. The illumination level is controlled manually and increased until saturation of the SPV signal is reached. CPD data are collected with a custom LabView program and monitored in real time.

The second system is very similar, but is placed inside a humidity and oxygen controlled glovebox (ideally  $< 5\text{ppm O}_2 \& \text{H}_2\text{O}$ ) and will therefore be referred to ‘Glovebox Probe Station’ or ‘Glovebox 301’<sup>4</sup>. Mounting and electrical connection of the sample are virtually identical to the Ambient Probe Station, but illumination offers more flexibility. On the one hand, an identical illumination set-up, also using a xenon-lamp and VariAC source can be used. On the other, the system is fitted with a more advanced illumination scheme to allow for Surface Photovoltaic Spectroscopy (SPS) measurements over a spectral range spanning IR to ultraviolet (UV) radiation. These capabilities were not used in this project and so shall not be further described. For the purposes of this project, the Ambient and Glovebox probe stations are practically identical and offer a trusted source of comparison for CPD and SPV data taken with the new, to be developed system. Influences of the atmosphere, viz. clean nitrogen vs. ambient, were investigated but were found to be negligible compared to the unavoidable experimental uncertainties in CPD and SPV measurements.

### 2.3.2 The Lakeshore Cryogenic System coupled with a Mc Allister Kelvin Probe

Lakeshore is an international vendor of cryogenic probe stations. For this research, a Lakeshore Model TTPX Probe Station was used. The probe station can be thought of as being divided into four components. An outer vacuum-chamber is connected to a pump to reduce the pressure inside the station. An Argon gas inlet connected to the vacuum chamber can be used to provide an inert atmosphere. Inside the vacuum chamber is a separate, smaller chamber: the radiation shielding stage, primarily used to shield the sample from IR radiation and thus used to facilitate measurements at low temperatures. The radiation shielding to some extend also provides electrical shielding from stray electrical signals and can therefore act as a quasi Faraday-cage. Both these chambers are fitted with windows to allow for placement of the probe-arms and to allow for visual inspection of the experiment. The radiation shielding stage’s windows is made from sapphire glass, as sapphire glass is oblique to infra-red radiation. Inside the shielding stage is placed the sample stage, which allows for mounting of samples and can provide an electrical ground. The fourth and last component of the probe station are its six probe-arms. They allow for placement of several probes on the sample from the outside. For many measurements, these probes are conceptually simple gold wires which allow for electrical measurements of the sample, such as IV and CV characterisation. Being a cryogenic system, the Lakeshore is fitted with three thermocouples. They measure the temperature of the sample stage, the radiation chamber and the probe-arm respectively. The temperature is adjusted by an electrical heater and by controlling the flow of of coolant, either liquid nitrogen or – to achieve lower temperatures – liquid helium. Evacuation of the cryogenic system is achieved by a combination of two pumps: a ‘weak pump’ to reduce the pressure to  $\sim 5 \cdot 10^{-2}$  and a ‘turbo pump’ to reduce it down to  $\sim 5 \cdot 10^{-4}$ . A schematic of the Lakeshore model TTPX cryogenic system showing its components is given in Figure 2.3.

In our case, one of the probe arms is fitted with a modified Mc Allister ultra-high vacuum (UHV) Kelvin probe head. The original Mc Allister UHV Kelvin probe head is

<sup>4</sup>The glovebox and its probe station are situated in room 301 on a different floor than the other experimental facilities of the Cahen group.

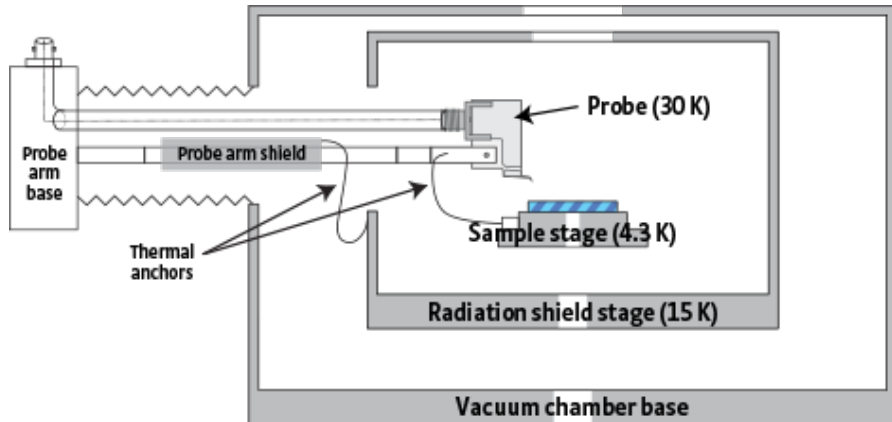


FIGURE 2.3: Schematic of the Lakeshore model TTPX cryogenic system and its components, typical operational temperatures are indicated. Taken from the vendor's website [3].

a horizontal base-arm ending in a vibrating, stainless steel cylinder of 2.6 mm diameter ending in a continuous, flat disk. This disk forms one of the two capacitor plates necessary for a CPD measurement. The other capacitor is, of course, the sample. Using the Mc Allister, the measured signal is given by equation (2.1) i.e. the signal is equal to the work function of the probe head, usually  $\sim 4.5$  eV, minus the work function of the sample. A reduction in measured CPD therefore means an increase in the sample's work function. The original probe head configuration is not suitable for the Lakeshore cryogenic system because the sample needs to be placed horizontally onto the sample-stage. Therefore, a vertical geometry is needed for the probe-head. Such a custom system was provided by Mc Allister. The stainless-steel Kelvin probe head is now vertically mounted in a plastic base. The size and especially the weight-distribution of the original cylinder are carefully designed by Mc Allister to comply with a vibration-response that is suitable for the probe head controller. The probe head is electrically connected by a gold wire that runs along the base-arm and is either soldered directly onto the cylinder or tightly wrapped around a conductive screw which is used to hold the probe head in place in its plastic holder. In the latter case, conductive silver paste suitable for UHV environments is applied to the screw to ensure low resistance electrical connection. Contact potential difference measurements are severely negatively affected by non-ohmic back contacts. A second probe arm of the cryogenic system was fitted with an optical fibre to allow for laser illumination of the sample. However, in practice, it quickly became clear that such an illumination set-up was unsuitable for SPV measurements. This was due to several reasons. For suitable CPD measurements, the probe head needs to be brought in very close proximity to the sample: distances on the scale of a few hundred micrometers are often necessary to obtain a sufficiently noise-free signal<sup>5</sup>. Therefore, there is simply not enough room for the exit of the optical fibre to be placed in a position where light would illuminate the sample. A further difficulty of the fibre illumination scheme are noticeable reductions in light intensity due to absorption in the fibre. After all, the fibre needs to be able to withstand vacuum conditions and low temperatures, limiting the choice of suitable materials. Lastly, the fibre would provide a very localised spot of illumination. For a successful measurement of the SPV, the whole area under the probe head has to be

<sup>5</sup>This adds to the practical danger of involuntarily crashing the vibrating probe head onto the sample, potentially damaging the sample, contaminating the probe head and generally interfering with conducting an experiment

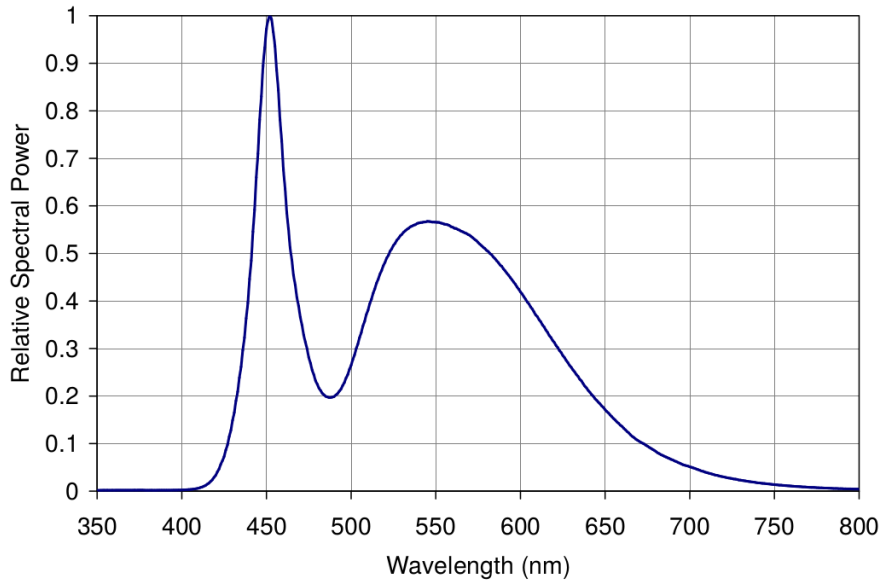


FIGURE 2.4: Typical relative spectral intensity of the LEDengine LED at an operating temperature of 25 °C, taken from the vendor’s supplementary information [4, p. 10].

saturated by illumination at the very least. Full saturation of the whole sample surface is in most cases desirable to suppress unwanted carrier recombination in the dark areas. For these reasons, it was decided to modify the probe head and employ a different illumination scheme. The cryogenic system’s windows allow for illumination by a source of light placed outside the vacuum chamber, on top of the external window, focused onto the sample surface. To allow this scheme to work, the main body of the probe head needed to be hollowed out and holes needed to be drilled into the head’s disk to let light pass through and onto the sample. Such a probe head, manufactured from stainless steel, was provided by Mc Allister and used in initial experiments. When successful measurements were not forthcoming, three further modifications of the probe head were tried, all based on the same principle. The idea was to replace the massive disk with a wire-grid used for transmission electron microscopy (TEM). Three different types of wire-grids were purchased from Structure Probe Inc., a stiff, stainless steel grid with 70 % opacity, two thin, flexible gold grids with 70 % and 60 % opacity respectively. The grids were laser-welded onto custom-made, hollowed out stainless steel cylinders. These new probe heads were manufactured by the Weizmann Institute’s Department for Construction and Engineering. Care was taken to ensure acoustic vibration characteristics of the new probe heads were similar, if not identical to those of the original Mc Allister probe heads. The wire-grids would add two benefits: they would increase the overall transmission of the probe head as well as allow for a more even illumination of the sample surface. In practice, however, no immediate, significant difference between the performance of the original hollow stainless steel probe head and the new, TEM wire-grid heads was found. At this point, an inherent limitation of the adopted illumination scheme has to be pointed out: namely that even in the ideal case, illumination from above will only result in an illuminated area directly under the probe head. The probe arm, probe head holder and even the edge of the hollow cylinder will all cast a shadow on the sample, especially since they need to be placed directly above it.

In order to allow for saturating illumination of the sample, the choice of light source

is crucial and it was thus a main focus of this part of the project to identify such a source and to successfully connect it to the combination of Lakeshore cryogenic station and Mc Allister Kelvin Probe. Successful SPV measurements are routinely carried out in the group using the Ambient Kelvin Probe Station and its xenon-lamp. The xenon-lamp is not only a source of light, but also a source of heat and thus unsuitable for the temperature-dependent measurement inside the Mc Allister. Not only would the heat introduce uncertainties in temperature but temperature gradients introduced by it could also damage the cryostation, specifically the radiation shielding stage's sapphire window. Therefore, the choice fell upon a high intensity, natural-white light emitting diode (LED) manufactured by LED Engin, model LZP-00CW0R. The LEDEngin LED uses 25 LED-spots soldered onto and electrically connected by a printed circuit board (PCB). Using thermo-paste, the LED is mounted onto a copper-core of a discarded computer fan. The fan is driven by a motor that uses a small 12V AC current source to achieve the necessary cooling of the delicate LED. As purchased, the LED has a relatively wide illumination cone of  $60^\circ$ , due to an internal fish-eye lens that is situated right atop the PCB. Therefore, the lamp was supplemented by a total internal reflection lens by LEDEngin that focuses 90 % of the illumination into a  $10^\circ$  wide cone. The initial LED of nominally 4200 lm intensity was damaged, only 12 of 25 LED-spots were functioning and was later replaced by new LED of the same manufacturer with 5400 lm intensity. The LED is driven by a variable DC source at a maximum voltage of 18.2 V and maximum current of 1.5 A. Its relative spectral intensity is given in Figure 2.4.

## 2.4 Measuring CPD at room temperature

### 2.4.1 Sample Preparation

A fresh surface of HOPG is prepared by gently rubbing adhesive tape onto a square piece of HOPG and tearing it off evenly. The piece is mounted onto a sample-holder using an electrically conductive clip and the CPD is measured.

n-Si-H (100) with different resistivities/doping-levels is prepared according to a slightly modified standard cleaning procedure: pieces of suitable size are cut with a diamond tip cutter, swiped off with ethyl-acetate and successively sonicated for three minutes each in ethyl-acetate, acetone, methanol and water. The pieces are microwave-treated in an O<sub>2</sub>-plasma at 100 W with a flow of 1 cm<sup>3</sup>/min O<sub>2</sub> and 1.5 cm<sup>3</sup>/min Ar for 3 minutes. Subsequently, samples are rinsed with pure water (18 MΩ cm at 20 °C), immersed in 2 % HF etching solution for 1 minute, rinsed with water and ashered again as before. The pieces are etched as before, back-contacts are created by applying InGa-eutectic to a scratched back surface. The piece is mounted onto a sample holder and the CPD is measured for at least two minutes each on three different spots per piece. The time the sample is subjected to ambient after etch and before each measurement is recorded and used in a linear fit ' $\Delta(\text{CPD})/\Delta t$ ' to serve as an indication of the CPD each spot on each piece would have had right after the etch, i.e. without the time needed for creating the back surface, mounting the sample and measuring other spots.

### 2.4.2 Results & Discussion

The standard deviation of measured CPD between spots of the same piece is comparable to that between pieces, so all obtained values were averaged. The values obtained across the three systems agree very well with each other and in the case of mid- and high-resistivity silicon also with theory, see Figure 2.5. A three, instead of only one,

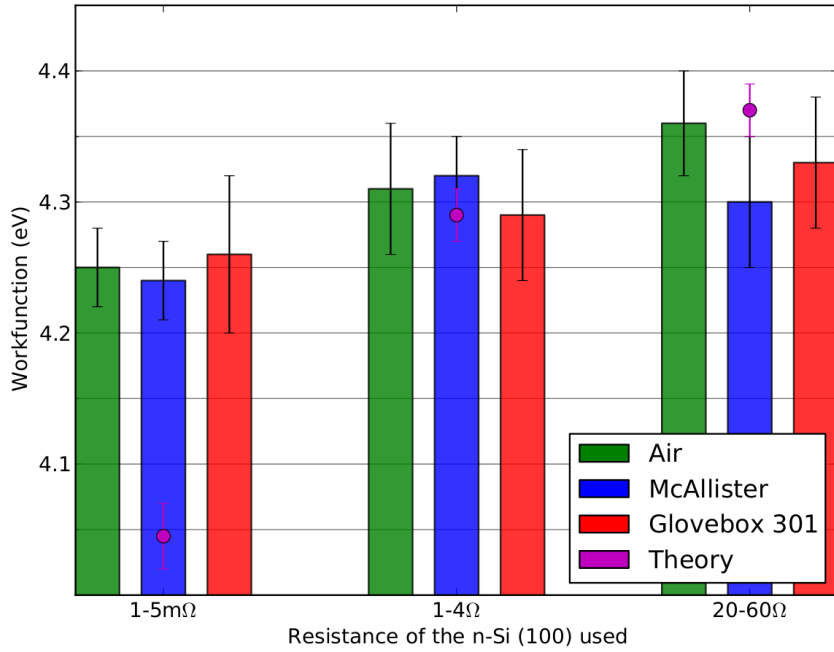


FIGURE 2.5: Summary of the calculated work functions for the n-Si-H samples used. There is good agreement between the different systems and good agreement with theory, except for the case of low resistivity, highly doped silicon. Indicated errors include deviations in the samples & the inaccuracy of calibration with HOPG.

minute long HF etch did not influence the CPD obtained for the low resistivity sample. A possible explanation for the deviation from theory might be found in the increased surface-reactivity of highly doped silicon: by the time the experiments are started, the silicon surface might already be oxidised.

## 2.5 CPD as function of pressure and temperature

### 2.5.1 CPD as a function of pressure

Once it was established that results obtained from the three independent system under similar conditions using hydrogenated silicon as a reference sample, efforts were concentrated on temperature and pressure dependent measurements in the Lakeshore cryogenic system. Because of unavoidable contamination with oxygen from ambient, hydrogenated silicon was not used to that end. Instead, a freshly prepared reference of HOPG was placed on the ground of the radiation shielding stage without a sample-mount. An electrically conductive screw and clip were used to connect the top of the HOPG sample to the electrical ground of the Lakeshore. Two sets of experiments were carried out to independently determine the influence of pressure and temperature on the measured CPD. In the first set, the measurements was commenced under ambient condition and allowed to continue for some time. The probe head was then retracted to avoid crashing it onto the sample and the weak pump was turned on. The probe head was then brought into proximity of the sample to continue the measurement and the measurement was allowed to continue for some time. The probe head was retracted again and the turbo pump was switched on. Again, the probe head was lowered to continue with the

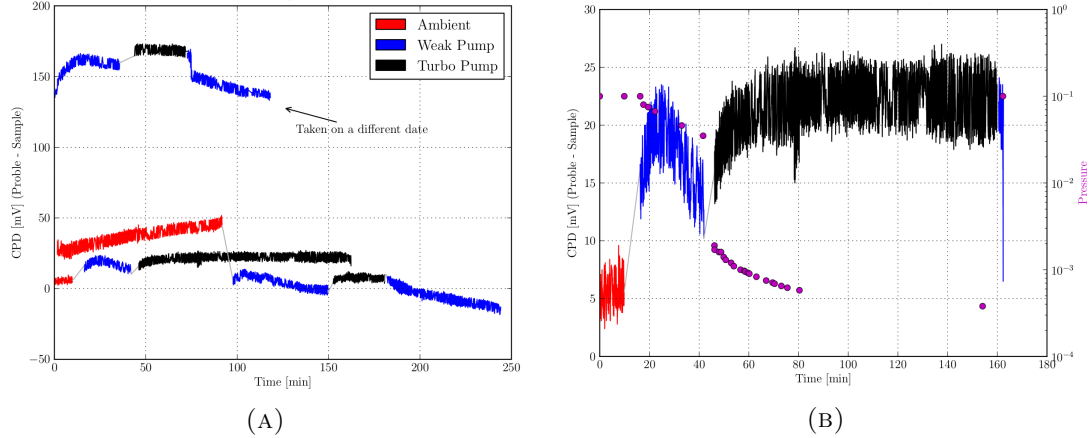


FIGURE 2.6: Raw data obtained from a measurement of the CPD during pressure reduction in the Mc Allister cryogenic system. Figure 2.6a shows results obtained from independent measurements of a piece of HOPG carried out on different days. It is indicated which pump was active to reduce the pressure inside the sample chamber. Figure 2.6b gives more detail about one of these measurements and actual measurements of the pressure at different stages during evacuation.

measurement and the measurement was allowed to continue for some time. For results of this experiment, see Figure 2.6. This experiment revealed several features. Firstly, the CPD of HOPG rises as a function of time under ambient condition. This is readily explained by oxygenation and/or other sources of contamination from ambient, such as water for example. Once the weak pump is turned on, there is a discontinuity in CPD. This discontinuity is not systematic in its direction, it may change the CPD either 'up' or 'down' and can therefore best be explained by a displacement of the probe head over the sample. The sudden reduction in pressure exerts a force on the probe arm and may cause it to move slightly. The size of the discontinuity is within the size of variation of CPD observed when different spots of the same reference are measured. The CPD now reduces as a function of time and this may be explained by gradual decontamination of the sample: as the pressure reduces, previously adsorbed contaminants may leave the surface. A second viable explanation may be a gradual change in acoustic vibration characteristics as a result of the reduction in pressure. To distinguish between the two, an experiment was performed in which the sample chamber was flushed with clean, inert Argon after having been subjected UHV conditions for about 20 minutes. It is assumed that complete desorption of possible contaminants is achieved by this treatment and that the high purity argon does not introduce fresh contaminates. The pressure was then again reduced using the weak pump and the CPD again reduces as a function of time. We therefore conclude that the observed reduction in CPD is indeed caused by gradual changes in pressure rather than desorption of contaminants. It is thus advisable to carry out CPD experiments under conditions of stable pressure, especially given the fact that the probe head is specifically designed by Mc Allister to carry out ultra-high vacuum CPD measurements.

### 2.5.2 CPD as a function of temperature

To determine the possible influence of temperature on the quality and reliability of the measurement, an ultra-thin layer of aluminium was deposited onto a piece of silicon by atomic-layer-deposition and a natural layer of surface oxide was formed. Alumina was chosen as a surface of interest because of its natural affinity for water. If contamination by water and subsequent freezing of the surface is an inherent problem of low temperature CPD measurements, then a strongly hydrophilic surface should exhibit these problems. A fresh wafer of silicon with 20 nm of aluminium by ALD was cut into suitable pieces. Pieces were swiped off with ethyl-acetate and sonicated for three minutes in iso-propanol, blow-dried under N<sub>2</sub> and subsequently microwave-treated in an O<sub>2</sub>-plasma at 100 W with a flow of 1 cm<sup>3</sup>/min O<sub>2</sub> and 1.5 cm<sup>3</sup>/min Ar for 3 minutes, ensuring a clean alumina surface. The back-side was scratched and InGa-eutectic was applied to create a back-contact. The work-function of this surface was measured in the ambient probe station and found to be  $(4.00 \pm 0.12)$  eV. To ensure an ohmic back-contact, the sample stage of the Lakeshore was lightly scratched and a small quantity of InGa-eutectic was applied to the stage. The piece was then placed on the sample stage and slight pressure was applied. The stage was introduced into the Lakeshore cryogenic system and the pressure was reduced. Using liquid nitrogen and the heaters, the temperature was reduced to 250 K and allowed to stabilise. Under these conditions, the work-function of the alumina surface was found to be  $(4.17 \pm 0.15)$  eV <sup>6</sup>. It has to be pointed out that the sample surface is not the coldest point inside the Lakeshore's inner chamber. Because of the way liquid nitrogen is introduced into the system, the radiation chamber's ground surface is the coldest. Therefore, it can be assumed that any ice would form there rather than on the sample, corroborating the result presented above.

### 2.5.3 Conclusion

CPD measurements using the Lakeshore are feasible when the pressure is constant. They may be carried out under ambient pressure with an inert argon atmosphere or under ultra-high vacuum conditions. A changing pressure is not conducive for reliable measurements of the contact potential difference but under conditions of stable pressure, CPD values obtained from the Lakeshore agree with values obtained from the other probe stations. Lowering the temperature below the freezing point of water does not pose an inherent restriction on the feasibility of CPD measurements in the Lakeshore system. The observed CPD was in agreement with experiments carried out at room temperature. In agreement with the literature [23, 24, 25, 26, 27] possible fluctuations of the work function of the probe head are small compared to other sources of experimental uncertainty and the WF can indeed be taken as a constant.

## 2.6 Measuring the SPV at room temperature

A necessary condition for the successful determination of the SPV of a sample is saturation with light. In practice, this means that the light-intensity during a measurement of the SPV is gradually increased up to the point where further increase in intensity does not lead to further increase of the measured surface photovoltage. Detailed interpretation of the measured signal is often problematic and requires intimate knowledge of the sample and even theoretical discussions of the SPV tend to be very involved. However,

<sup>6</sup>A suitable piece of HOPG was also present in the sample chamber to allow for calibration of the work-function of the probe head

from the point of view of establishing whether a new experimental set-up is suitable for more advanced SPV-measurements, a successful, saturated measurement of the SPV of a relatively simple test-sample is a necessary precondition. To that end, SPV measurements of an alumina surface were chosen as a test case. Alumina was chosen for its stability, relative simplicity and because of its relatively large SPV signal. The sample is the same as used for the determination of the temperature dependence of the CPD: 20 nm aluminium deposited by ALD onto a wafer of silicon. The preparation and cleaning protocol of the sample is the same as above: rinsing; sonication; oxidation and creation of an ohmic back-contact using InGa-eutectic. The sample's SPV was determined in the ambient probe station as is<sup>7</sup> and was found to be  $(530 \pm 20)$  mV. To check if the LED is a suitable source, it was installed in the ambient probe station and an SPV measurement was carried out. To facilitate the comparison between the systems, the ambient probe station's light focusing lens was removed as no such lens could readily be installed with the Lakeshore. Since the LED has a variable electrical source, it was possible to increase the current through the LED from 1 A to 1.6 A in steps of 0.1 A. In a set of preliminary experiments not reported here, it was established that the illumination intensity of the LED as determined from a standard silicon test-cell does indeed increase smoothly over the appropriate current range when combined with the Kelvin probe stations as described. The sample was introduced into the Lakeshore's inner chamber and the LED was placed on top of the vacuum chamber's outer window. The current through the LED was increased in the same steps as for the measurement in ambient and the results of the experiment are summarised in Figure 2.7. In that Figure 'Upstairs' refers to the measurement in the ambient probe station, 'Downstairs' refers to the measurement with the Mc Allister probe head, 'old' refers to the initial LED with only 12 of 25 spots working and 'new' refers to the newly purchased LED in which all diodes are working and which achieves a maximum illumination of 5200 lm. It has to be pointed out that the new LED could be driven further than up to a maximum of 1.0 A to reach its full illumination intensity at a maximum current of 1.6 A, so the experiment was extended to make use of the maximum achievable intensity. As can be seen, saturation of the SPV is readily achieved with the LED in ambient at a current of 0.6 A and the measured value of  $(540 \pm 10)$  mV is in good agreement with the value expected from the measurement of the SPV with a xenon light source. It is furthermore apparent that the measurement achieves saturation. At a current of about 0.8 A, a further increase in current does not result in a corresponding significant increase in measured surface photovoltage. However, there is a significant discrepancy of 60 mV<sup>8</sup> in measured SPV between the two systems which cannot readily be explained. A similar experiment using neutral density filters to control the light intensity was carried out, but no meaningful conclusions could be drawn from the results, so it is not presented here. In a following step, the SPV of the alumina sample was measured with the Lakeshore not completely assembled. The vacuum chamber's lid as well as the radiations shielding chamber's lid were removed and the LED was held by hand as close to the probe head as possible without interfering with the measurement<sup>9</sup>. This configuration obviously does not represent a working condition for the Lakeshore, nor is it readily reproducible because of its vague parameters, but an SPV of  $\sim 480$  mV could be achieved in this way. At this point, the nature of the 60 mV discrepancy remains unknown. It might be due to the increased distance between the source and the sample or it might be due to partial absorption by the Lakeshore's

<sup>7</sup>i.e. ambient probe station and xenon light source

<sup>8</sup>about 10 % of the maximum signal

<sup>9</sup>a constant stream of argon was employed to avoid undue contamination of the inner chamber from ambient.

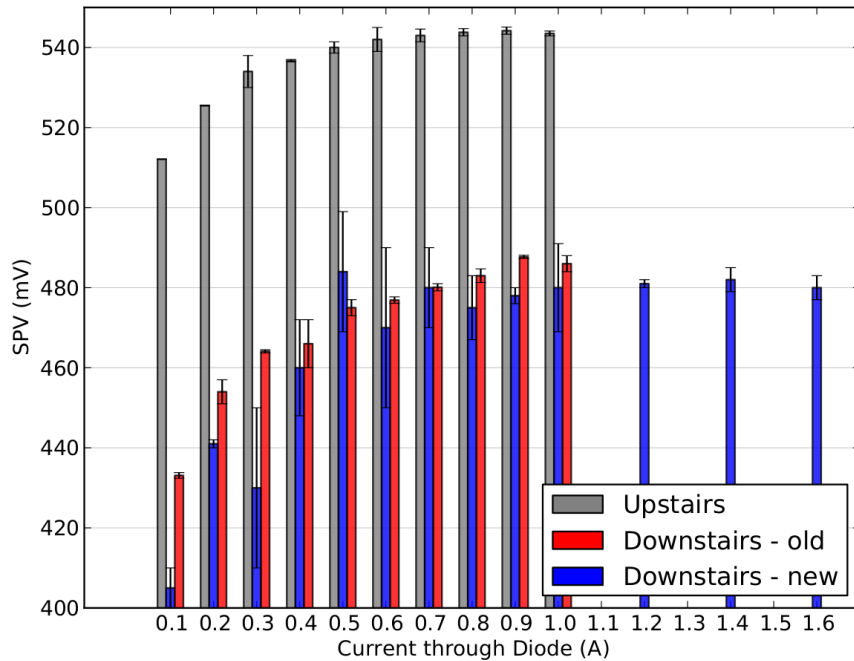


FIGURE 2.7: Comparison of the measured SPV as a function of illumination level as evidenced by the current through the LED. ‘Upstairs’ refers to the combination of LED and the ambient probe station, while ‘Downstairs’ refers to measurements with the LED, the Mc Allister cryostation and the custom Lakeshore KP probe head. ‘Old’ signifies the weaker, damaged LED of nominally 4200 lm intensity, while ‘new’ refers to the fully functional LED of 5400 lm intensity. Note that the measurement saturates independent of illumination intensity (‘old’ vs. ‘new’) at a lower measured SPV than the comparison with the ambient probe station.

windows, especially the IR-shielding sapphire glass but the results obtained here remain hard to interpret properly. Saturation is achieved, but not at the right level. Simply using a stronger source will therefore most likely not alleviate the problem. It may be tried to replace the windows by lenses which better focus the light beam onto the sample but is questionable if such a scheme is practically feasible or indeed even helpful. Practically, such window-lenses would have to be able to withstand UHV conditions and saturation was achieved in ambient even without a lens, where the distance between sample and source is comparable to the corresponding distance in the cryogenic system. Since no explanations of the source of the discrepancy between the systems are forthcoming, a systematic experimental uncertainty of underestimating the SPV by about 10 % has to be assumed when using the Lakeshore in conjunction with the LED.

## 2.7 Temperature dependent measurement of the SPV

Since it was established that temperature dependent CPD measurements could reliably be carried out and that, albeit with a systematic uncertainty, SPV measurements could also be carried out with the Lakeshore cryogenic system, the final step was to attempt a combined experiment and carry out a temperature dependent measurement of the surface photovoltaic. To this end, a suitable sample needed to be identified. This sample should have a sufficiently large photo-response and should undergo some phase transition at a well defined, critical temperature. Three different systems were investigated: biological samples consisting of a plant's photo-system immobilized on a gold surface; a lead-iodide-chloride perovskite on titanium-dioxide and finally a thin layer of vanadium oxide.

The biological samples exhibited changes in CPD on the order of 20 mV. These changes occurred at a well defined temperature, from 250 K to 260 K. While interesting, these changes but were too small to serve as a reliable system for a proof of principle: 20 mV is within the experimental uncertainty of both the CPD and the SPV measurements. The biological samples were therefore quickly abandoned.

For the perovskites, it was attempted to compare their reaction when exposed to different parts of the optical spectrum, namely to compare their dark CPD to the CPD when exposed to full spectrum illumination and when exclusively exposed to infra-red illumination. The perovskite sample was introduced to the inner chamber of the Lakeshore and electrically contacted with the help of a conductive clip and screw. To allow for electrical connection via the back contact, the perovskite was removed from the point where the clip contacted the sample. The cryogenic system was evacuated and seven temperatures were chosen at which to measure the CPD: 130 K, 170 K, 210 K, 230 K, 250 K, 270 K and 280 K. At each of these temperatures, the dark CPD was measured. A filter which would only allow IR radiation to pass was placed in front of the source, the sample was briefly illuminated and the IR CPD was measured. The CPD of the system was allowed to decay back to its original dark value and the filter was removed. The system was then briefly illuminated by full spectrum at high intensity and the light CPD was measured. The CPD of the system was allowed to decay back to its original dark-value and the system was then cooled down to the next temperature step. In the course of this measurement, repositioning the probe head to new positions over the sample was necessary because although care was taken, crashing the probe head onto the sample could not be avoided. The whole experiment was carried out under low pressure conditions, but for the lowest five temperature points, the pressure was about a factor ten lower than for the measurements taken at 270 K and 280 K. To carry out the

experiment, the set up of the Mc Allister had to be modified twofold. Measurements had to be carried out without the inner chamber's sapphire glass window as this would exclude any infra-red radiation from reaching the samples in the first place. Secondly, the xenon lamp had to be used as a source of illumination to give access to the infra-red part of the spectrum. These modifications introduced experimental difficulties for several reasons. As already pointed out, the xenon lamp is a source of heat and therefore, an unknown experimental uncertainty in the temperature was introduced. The experiment had to be carried out very quickly to avoid damage to the system and to minimize said uncertainty in temperature. In effect, only a brief flash of illumination could be allowed to reach the sample. Furthermore, the xenon lamp and its high power electrical source had to be set up in close proximity to the Lakeshore cryogenic system and electrical noise due to the relatively high currents and voltages involved in this experiment were introduced. To add to these problems, the sample was neither fresh nor necessarily stable and perovskites are inherently complicated systems. Accordingly, the results did not show a clear variation with temperature and could not be reproduced on consecutive days. Therefore, it was decided that this experiment could not serve for the purpose of showing a reliable SPV(T) measurement.

### 2.7.1 Vanadium oxide

#### Description of samples and preliminary research carried out at the Cahen group

Vanadium-dioxide ( $\text{VO}_2$ ) is a system well known for undergoing a metal to insulator transition (MIT) close to room temperature. At the heart of this transition lies a reconfiguration of the crystal lattice, where  $\text{VO}_2$  transitions from its high-temperature tetragonal (rutile) phase to a low temperature monoclinic phase. In the tetragonal phase, the Fermi level of the material is well within the conduction band and hence, the material behaves like a metal. In the monoclinic phase, an energy gap has developed and the material now behaves like an insulator [33]. Of course, the only difference between an insulator and a semiconductor is the size of their energy gaps and if the transition occurs gradually, one might also speak of a metal-semiconductor-insulator transition instead of an MIT. This transition has extensively been studied, using many different methods such as direct photoemission & x-ray absorption spectroscopy [34], Raman spectroscopy [35], ultra-fast pump-probe spectroscopy [36] etc. However, because of their relative simplicity, studies of the resistivity of the material stick out [37]. In these, changes of resistivity over several orders of magnitude are not uncommon. Finally, the MIT in  $\text{VO}_2$  was also investigated using Scanning Kelvin Probe Microscopy, where  $\sim 200\text{ nm}$  thin stripes of the material were grown adjacent to a strip of gold. These strips were continuously scanned over a temperature range including the phase transition temperature ( $T_{MI}$ ) of  $\text{VO}_2$ . Gold provided a stable reference work function and thus, the work function of  $\text{VO}_2$  could be measured in absolute terms. It was found that vanadium-dioxide has a work function of  $\sim 5.15\text{ eV}$  in its metallic phase and that the work function gradually decreased by  $\sim 0.15\text{ eV}$  over a range of  $60\text{ K}$  [38]. In other studies [39], it was found that MIT could be tuned by tungsten-doping of a thin film of  $\text{VO}_2$  grown on a supporting matrix of  $\text{TiO}_2$  and preliminary research into similar samples has already been carried out in the Cahen group.

The samples were either pure or 2% tungsten-doped vanadium-dioxide of thickness ranging from  $10\text{ nm}$  to  $80\text{ nm}$  grown on either  $\text{TiO}_2$  or on niobium-doped titanium-dioxide

(Nb:TiO<sub>2</sub>) and were kindly provided by M. Nakano of RKIEN. A change in resistivity of several orders of magnitude upon MIT could be shown for these samples. When used for this project, however, the collection of vanadium-dioxide samples had already been in storage inside a desiccator for more than a year. Many samples were damaged and proper storage throughout the year could not be guaranteed. Therefore, the choice of sample for this project was limited to pieces which, upon optical inspection, were closest to their initial appearance and were still large enough to allow proper positioning of the probe head over a sufficiently homogeneous surface. Therefore, a sample of 50 nm 2% W:VO<sub>2</sub> on pure TiO<sub>2</sub> was chosen. It had been investigated by Nir Kedem using the van der Pauw method with a temperature resolution <5 K. It showed an approximately two orders of magnitude change in resistivity with a relatively gradual profile, occurring over the temperature range from 220 K to 270 K. The resistivity also exhibited hysteresis, with up to half an order of magnitude difference in resistivity between cooling down and heating up.

### Experimental procedure, results and discussion

Initially, the work function of the vanadium-dioxide sample was determined with the ambient probe station. The sample was sonicated for three minutes each in acetone, ethanol and THF and was then blow-dried under N<sub>2</sub>. To calibrate the probe head, a fresh surface of HOPG was prepared and the CPD was measured. The work function of the probe head was found to be (5.085 ± 0.015) eV. The work function of the clean W:VO<sub>2</sub> sample was determined to be (5.17 ± 0.02) eV, in remarkable agreement with the value obtained by Ko *et al.* [38].

Before each measurement, the sample was subjected to the same cleaning procedure outlined above. The sample was then blow-dried under N<sub>2</sub> and placed directly on the ground of the inner chamber of the Lakeshore. Electrical contact was made from the top using a conductive screw and clip. The Lakeshore was then evacuated and the experiment commenced once a stable vacuum condition was obtained.

In the first experiment, the Lakeshore was cooled down to the lowest temperature achievable by liquid nitrogen cooling: 97 K for this cryogenic system. During this cool-down, the CPD was quickly measured at three points where the temperature remained relatively stable for a sufficient time. Once the lowest possible temperature was reached, the flow of nitrogen was stopped, the heater was set to 300 K and the CPD was measured continuously. This protocol allows for a quick measurement of the CPD(T)-response of the system to identify the temperature range of interest, but uncertainties in temperature are introduced because of the temperature gradient present in the inner chamber and because of having to note down the temperature manually. The experiment had to be aborted. The data obtained during this initial experiment are shown in Figure 2.8.

For the next experiment, the temperature range was extended and more care was taken to more accurately determine the temperature. The system was cooled down to 100 K and gradually increased. The CPD was measured at 11 well defined temperatures. For each of these temperatures, the flow of liquid nitrogen and the heater setting were carefully adjusted until all three of the cryogenic system's temperature read-outs were within a range of 5 K of each other. Holding the temperature constant, the CPD was then recorded once every second for a period of 100 seconds and these data were averaged. The temperature was increased to the next set-point and the procedure was repeated. The observations of this experiment are plotted in Figure 2.9. The uncertainty in CPD was taken to be twice the standard deviation of CPD values obtained during the 100 second period. Uncertainty in temperature is not shown but assumed to be less than 5 K.

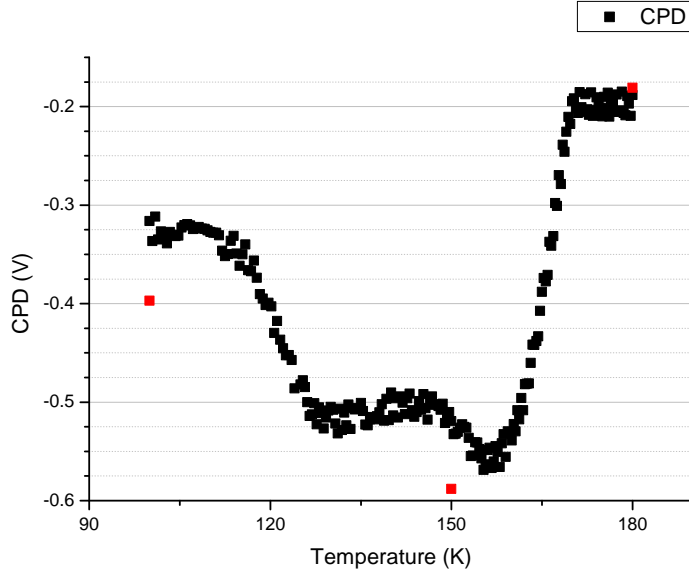


FIGURE 2.8: Raw data of the contact potential difference of the W:VO<sub>2</sub> sample obtained during a temperature-sweep. Data points in red were obtained while cooling down, data points in black were recorded while warming up.

In the last experiment, both dark and light CPD were measured for the same sample for a range of temperatures between 180 and 300 K in intervals of 20 K. CPD was only measured once the temperature gradient inside the Lakeshore was less than 5 K. For each temperature, dark CPD was measured once every second over a period of 100 seconds and these data were averaged. Illumination for light CPD was achieved by the LED at maximum intensity and to avoid possibly heating the sample, light CPD was measured for 15 seconds. HOPG as a reference for the work function was not used in this experiment. Instead, the work function of the sample at 300 K in vacuum was assumed to be the same as that obtained from the same sample at room temperature in ambient and the work function of the probe could therefore be calculated to be 4.41 eV. The results of this final experiment are shown in Figure 2.10. The experimental uncertainty in work function includes twice the standard deviation of dark CPD obtained during the 100 second interval plus an added uncertainty from the calculation of the work function of the probe head. The experimental uncertainty in SPV includes uncertainty from dark CPD as well as that for light CPD. Uncertainty in temperature is, again, not shown, but assumed less than 5 K.

Probably the most remarkable feature of these measurements is the sudden drop in CPD (sudden rise in WF) at  $\sim 120$  K and the consequent sudden rise in CPD around  $\sim 170$  K seen in both Figure 2.8 and Figure 2.9. Since these features were observed during cool down as well as during heating up in the first and were again observed in the second, independent measurement, they are most likely not an artefact of the measurement, nor should they be ascribed to simple experimental failure. They represent a change in work function of  $\sim 200$  meV to 400 meV which is remarkably large. Such changes can most likely not be explained by changes in shielding of accumulated surface-charges or repositioning of the Fermi level. A (reversible) surface-reconstruction or even a (reversible) change of chemical composition might be able to explain the data, but without further measurements, we cannot be sure. To the best of my knowledge, neither

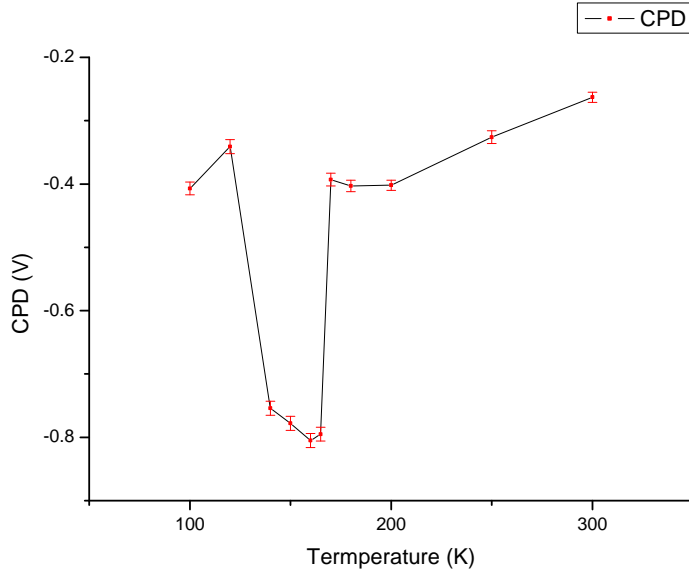


FIGURE 2.9: The contact potential difference of the W:VO<sub>2</sub> sample as a function of temperature. Experimental uncertainties are explained in the text.

a structural reconstruction nor a change in WF at the temperatures in question has yet been reported in the literature for W:VO<sub>2</sub>. In conjunction with the measurements carried out by Nir Kedem, the experiments reported in the literature and those summarised in Figure 2.10, it has to be assumed that the changes in WF seen at around 120 K and 170 K are not explained by the known MIT of vanadium-dioxide. The difference in CPD between heating up and cooling down seen in Figure 2.8 might be taken as evidence for hysteresis at lower temperatures than previously observed, but the data is sparse, so no conclusive explanation can be drawn from them. Figure 2.9 on the whole corroborates what was observed in the initial, relatively inaccurate experiment even though the size of the observed effect is greater, but nothing more can be concluded from these measurements alone.

We will now concentrate on the measurement of the SPV as shown in Figure 2.10. A significant SPV is observed below 280 K, at 240 K the SPV is at its maximum of  $\sim 120$  mV and below 220 K SPV is reduced back to levels comparable to those at room temperature. A significant SPV signal is therefore observed in the same temperature range that was identified for MIT in the resistivity measurements. In the metallic rutile configuration, no SPV is observed and none is expected. As the energy gap of the material gradually widens, the SPV gradually increases because gradually less thermally free carriers can shield trapped surface charges in the dark condition. The simultaneous presence of both phases of vanadium-dioxide over a range of temperatures has been observed in the literature [40]. As a result, band bending and hence observed SPV gradually increase. If the SPV is assumed to be saturated at 240 K and, accordingly, the bands to be flattened, the band bending is  $\sim 120$  meV. Possible Fermi level pinning would add to the size of the band bending, so the stated value has to be seen as a minimum. On first sight, the gradual decrease in SPV signal might be puzzling. One would expect the trend for the SPV to continue, after all, the idea behind low temperature SPV is to counteract thermally free carriers and increase the influence of electron-hole pairs created by absorption of light. However, the observation made here can be explained if one

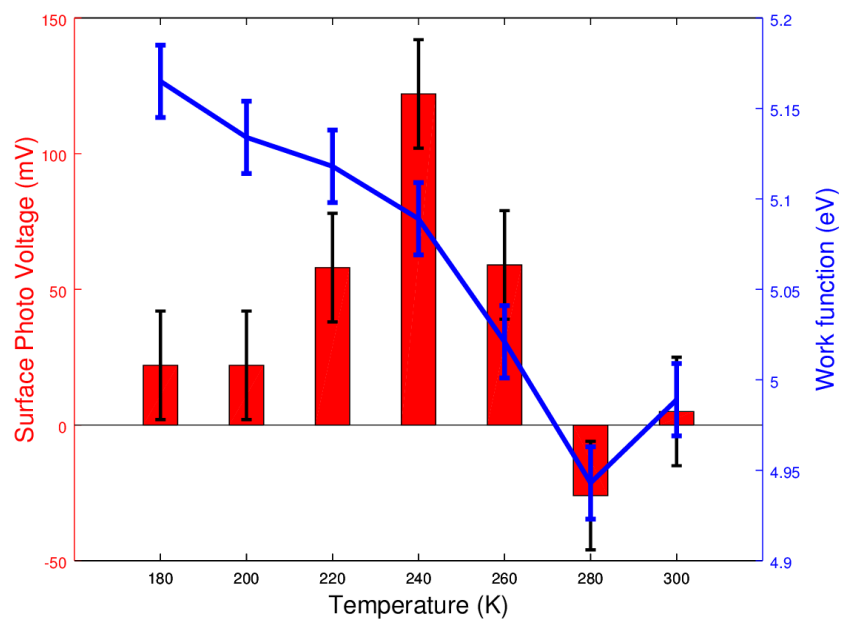


FIGURE 2.10: Measured surface photovoltage and calculated work function for the W:VO<sub>2</sub> sample as a function of temperature. The appearance of an SPV coincides with the MIT temperatures observed in earlier measurements, its positive sign indicates an n-type semiconductor. The change in WF is substantial but remains unexplained without further experiments. Experimental uncertainties are explained in the text.

recalls that vanadium-dioxide is undergoing a metal to *insulator* transition and that for an insulator, the energy gap is expected to be relatively large. Looking at the spectrum of illumination, Figure 2.4, a clear cut off below 400 nm is seen. 400 nm radiation corresponds to a photon energy of  $\sim 3.1$  eV so if the energy gap in VO<sub>2</sub> becomes larger than this, no carriers can be created by illumination or rather: only a minute fraction of incident photons corresponding to the minute fraction of photons at the low-wavelength tail of the LED will have sufficient energy to create free carriers. Therefore, the sample is no longer saturated by illumination and a significant drop in observed SPV signal is expected. A problem with that interpretation is that the band gap of vanadium-dioxide is consistently reported as  $\sim 0.7$  eV, from theoretical [41] as well as from experimental studies [42, 36, 34, 43].

Concentrating on the temperature range 180 to 300 K, a change in WF of  $\sim 150$  meV is seen in both in Figure 2.9 and, more clearly, in Figure 2.10. So far, positive changes of WF of up to 450 meV have been observed for bundlelike VO<sub>2</sub> nanostructures [44]. A change of  $\sim 150$  meV was also reported by Ko [38] during the MIT of vanadium-dioxide, but they observed a decrease instead of the increase in WF seen here. The difference between the sample used in their research and the one used here is the presence of tungsten as dopant. Tungsten has more valence electrons than vanadium even in its elemental state and certainly has more valence electrons than vanadium in its oxide. Tungsten should therefore act as n-type dopant. This is in accordance with the sign of SPV observed in Figure 2.10. The change in WF can not be explained by a gradual change in the position of the Fermi level: for an n-type material,  $E_f$  is expected to increase with lowering temperature. The carrier concentrations inside the material might change drastically due to dopant freeze-out or other mechanism and that might change  $E_f$  sufficiently to account for the rise in WF, but without further experiments, these attempted explanations remain speculative. In fact, there is doubt in the literature if a simple ‘gap opening process’ can indeed explain the observed MIT [45, 46]. Judging by the complexity of the material, attempts at explaining the observed data in terms of simple band diagram considerations of typical metals and n-type semiconductors will fall short. Similar experiments with an extended spectral range or a more detailed study of spectral surface photovoltaic might serve to verify the results obtained for this material here, but they are out of scope of this project: elucidating the finer details of the MIT observed in W:VO<sub>2</sub> was not the aim of this project. Vanadium-dioxide was, above all, chosen as a system to show a viable SPV(T) measurement, to serve as a proof of concept for measuring temperature dependent SPV with the Lakeshore cryogenic system. This was achieved with these experiments.

## 2.8 Conclusion

A series of experiments showed the viability of using the Lakeshore cryogenic system equipped with a Mc Allister Kelvin probe head and an LED illumination source as a system to measure temperature dependent changes in the surface photovoltaic. To do so, the CPD obtained under various circumstances, namely in ambient, under low pressure and at temperatures below freezing was compared to existing, trusted systems. Deviations between the systems were within normal, acceptable experimental uncertainties usually encountered when using Kelvin Probe measurements. The SPV obtained from measurements in the Lakeshore at room temperature was shown to agree with SPV measurements carried out in the ambient system and lastly, experiments to show a viable SPV(T) measurement were carried out. Some aspects of these experiments were

shown to be in good agreement with earlier, preliminary research carried out in the Cahen group and with results reported in the literature while the finer detail and precise interpretation of all the observed features remains elusive without further investigations. However, with vanadium-dioxide, it could be shown that interesting and reproducible data can be obtained by using the Lakeshore cryogenic system for CPD(T) and SPV(T) measurements.

# List of References

- [1] Charles Kittel. *Introduction to Solid State Physics*. John Wiley and Sons, Inc., eigths edition, 2005.
- [2] Mel M. Schwartz, editor. *Encyclopedia of Smart Materials*, volume 1 and 2. John Wiley and Sons, Inc., 2002.
- [3] Lake Shore Cryotronics Inc. Model TTPX Cryogenic Probe Station. <http://lakeshore.com/products/cryogenic-probe-stations/model-ttpx-cryogenic-probe-station/pages/Overview.aspx>, 2015.
- [4] LED Engin. LZP-00CW0R. <http://www.ledengin.com/files/products/LZP/LZP-00CW0R.pdf>, 2015.
- [5] Peter Atkins and Julio De Paula. *Atkins' Physical Chemistry*. Oxford University Press, 8th edition, 2006.
- [6] Takeo Furukawa. Ferroelectric properties of vinylidene fluoride copolymers. *Phase Transitions*, 18(3-4):143–211, 1989.
- [7] Shuting Chen, Xue Li, Kui Yao, Francis Eng Hock Tay, Amit Kumar, and Kaiyang Zeng. Self-polarized ferroelectric {PVDF} homopolymer ultra-thin films derived from langmuir–blodgett deposition. *Polymer*, 53(6):1404 – 1408, 2012.
- [8] R Tadros-Morgane and H Kliem. Polarization curves of langmuir–blodgett pdvf-copolymer films. *Journal of Physics D: Applied Physics*, 39(22):4872, 2006.
- [9] Zhengguo Xiao, Qingfeng Dong, Pankaj Sharma, Yongbo Yuan, Baodong Mao, Wenjing Tian, Alexei Gruverman, and Jinsong Huang. Synthesis and application of ferroelectric P(VDF-TrFE) nanoparticles in organic photovoltaic devices for high efficiency. *Advanced Energy Materials*, 3(12):1581–1588, 2013.
- [10] Todd P. Silverstein. The real reason why oil and water don't mix. *Journal of Chemical Education*, 75(1):116, 1998.
- [11] O. D. Miller, E. Yablonovitch, and S. R. Kurtz. Strong internal and external luminescence as solar cells approach the Shockley-Queisser limit. *Photovoltaics, IEEE Journal of*, 2(3):303–311, July 2012.
- [12] Alexis Vossier, Baruch Hirsch, and Jeffrey M. Gordon. Is Auger recombination the ultimate performance limiter in concentrator solar cells? *Applied Physics Letters*, 97(19), 2010.
- [13] P.D. DeMoulin, S.P. Tobin, M.S. Lundstrom, M.S. Carpenter, and M.R. Melloch. Influence of perimeter recombination on high-efficiency GaAs p/n heteroface solar cells. *Electron Device Letters, IEEE*, 9(8):368–370, Aug 1988.

- [14] R.A. Sinton. Contactless carrier-lifetime measurement in silicon wafers, ingots, and blocks. <http://www.sintoninstruments.com/PDFs/WhitePaperHamburgFinal.pdf>, July 2009.
- [15] Henning Nagel, Christopher Berge, and Armin G. Aberle. Generalized analysis of quasi-steady-state and quasi-transient measurements of carrier lifetimes in semiconductors. *Journal of Applied Physics*, 86(11):6218–6221, 1999.
- [16] Ronald A Sinton and Andres Cuevas. Contactless determination of current–voltage characteristics and minority-carrier lifetimes in semiconductors from quasi-steady-state photoconductance data. *Applied Physics Letters*, 69(17):2510–2512, 1996.
- [17] Ronald A Sinton, Andres Cuevas, and Michael Stuckings. Quasi-steady-state photoconductance, a new method for solar cell material and device characterization. In *Photovoltaic Specialists Conference, 1996., Conference Record of the Twenty Fifth IEEE*, pages 457–460. IEEE, 1996.
- [18] Keung L. Luke and Li-Jen Cheng. Analysis of the interaction of a laser pulse with a silicon wafer: Determination of bulk lifetime and surface recombination velocity. *Journal of Applied Physics*, 61(6):2282–2293, 1987.
- [19] A. B. Sproul. Dimensionless solution of the equation describing the effect of surface recombination on carrier decay in semiconductors. *Journal of Applied Physics*, 76(5):2851–2854, 1994.
- [20] Seok Ju Kang, Youn Jung Park, Jinwoo Sung, Pil Sung Jo, Cheolmin Park, Kap Jin Kim, and Beong Ok Cho. Spin cast ferroelectric beta poly(vinylidene fluoride) thin films via rapid thermal annealing. *Applied Physics Letters*, 92(1), 2008.
- [21] Stephen Ducharme, V. M. Fridkin, A. V. Bune, S. P. Palto, L. M. Blinov, N. N. Petukhova, and S. G. Yudin. Intrinsic ferroelectric coercive field. *Phys. Rev. Lett.*, 84:175–178, Jan 2000.
- [22] R. C. G. Naber, B. de Boer, P. W. M. Blom, and D. M. de Leeuw. Low-voltage polymer field-effect transistors for nonvolatile memories. *Applied Physics Letters*, 87(20), 2005.
- [23] Mohamed Akbi. *On the Temperature Dependence of the Photoelectric Work Function of Contact Materials*, pages 463–467. VDE VERLAG GMBH, 2014.
- [24] Kh.I. Ibragimov and V.A. Korol'kov. Temperature dependence of the work function of metals and binary alloys. *Inorganic Materials*, 37(6):567–572, 2001.
- [25] C. R. Crowell and R. A. Armstrong. Temperature dependence of the work function of silver, sodium, and potassium. *Phys. Rev.*, 114:1500–1506, Jun 1959.
- [26] A. Kiejna. On the temperature dependence of the work function. *Surface Science*, 178(1):349 – 358, 1986.
- [27] A Kiejna, K F Wojciechowski, and J Zebrowski. The temperature dependence of metal work functions. *Journal of Physics F: Metal Physics*, 11(11):2495, 1981.
- [28] Zhen Zhang and John T. Yates. Band bending in semiconductors: Chemical and physical consequences at surfaces and interfaces. *Chemical Reviews*, 112(10):5520–5551, 2012.

- [29] Joy Dorene McNamara. The effect of temperature on the electrical and optical properties of p-type GaN. Master's thesis, Virginia Commonwealth University, 2011.
- [30] J. D. McNamara, A. A. Baski, and M. A. Reshchikov. Temperature-dependent Kelvin probe studies on GaN from 80 to 600 k. *physica status solidi (c)*, 11(3-4):726–729, 2014.
- [31] L Kronik. Surface photovoltaic phenomena: theory, experiment, and applications. *Surface Science Reports*, 37(1-5):1–206, 1999.
- [32] Besocke Delta PHI GmbH. Kelvin system. <http://www.besocke-delta-phi.de/kelvin.htm>, 2005.
- [33] M. Nakano, K. Shibuya, D. Okuyama, T. Hatano, S. Ono, M. Kawasaki, Y. Iwasa, and Y. Tokura. Collective bulk carrier delocalization driven by electrostatic surface charge accumulation. *Nature*, 487(7408):459–462, 2012.
- [34] T. C. Koethe, Z. Hu, M. W. Haverkort, C. Schüßler-Langeheine, F. Venturini, N. B. Brookes, O. Tjernberg, W. Reichelt, H. H. Hsieh, and H.-J. et al. Lin. Transfer of spectral weight and symmetry across the metal-insulator transition in VO<sub>2</sub>. *Phys. Rev. Lett.*, 97(11), 2006.
- [35] E. Radue, E. Crisman, L. Wang, S. Kittiwatanakul, J. Lu, S. A. Wolf, R. Wincheski, R. A. Lukaszew, and I. Novikova1. Optical properties differences across the insulator-metal transition in VO<sub>2</sub> thin films grown on different substrates. <http://arxiv.org/pdf/1210.7746v2>, January 2013.
- [36] Graham H. Jensen. Temperature-dependent femtosecond pump-probe spectroscopy of thin-film vanadium dioxide. Master's thesis, University of Rochester, 2014.
- [37] Keisuke Shibuya, Masashi Kawasaki, and Yoshinori Tokura. Metal-insulator transition in epitaxial v<sub>1-x</sub>w<sub>x</sub>o<sub>2</sub>(0=x=0.33) thin films. *Appl. Phys. Lett.*, 96(2):022102, 2010.
- [38] Changhyun Ko, Zheng Yang, and Shriram Ramanathan. Work function of vanadium dioxide thin films across the metal-insulator transition and the role of surface nonstoichiometry. *ACS Appl. Mater. Interfaces*, 3(9):3396–3401, 2011.
- [39] Keisuke Shibuya, Masashi Kawasaki, and Yoshinori Tokura. Metal-insulator transitions in TiO<sub>2</sub>/VO<sub>2</sub> superlattices. *Phys. Rev. B*, 82(20), 2010.
- [40] A. L. Pergament, G. B. Stefanovich, N. A. Kul'din, and A. A. Velichko. On the problem of metal-insulator transitions in vanadium oxides. *ISRN Condensed Matter Physics*, 2013:1–6, 2013.
- [41] S. Biermann, A. Poteryaev, A. I. Lichtenstein, and A. Georges. Dynamical singlets and correlation-assisted peierls transition in VO<sub>2</sub>. *Phys. Rev. Lett.*, 94(2), 2005.
- [42] Helena Prima Garcia. *Laser-induced structural changes at surfaces investigated with synchrotron radiation*. PhD thesis, Freie Universität Berlin, 2007.
- [43] P. Merenda, D. Kaplan, and C. Sommers. Near band gap optical absorption in semiconducting VO<sub>2</sub>. *J. Phys. Colloques*, 37(C4):C4–59–C4–62, 1976.

- [44] Haihong Yin, Min Luo, Ke Yu, Yanfeng Gao, Rong Huang, Zhengli Zhang, Min Zeng, Chuanxiang Cao, and Ziqiang Zhu. Fabrication and temperature-dependent field-emission properties of bundlelike VO<sub>2</sub> nanostructures. *ACS Appl. Mater. Interfaces*, 3(6):2057–2062, 2011.
- [45] Volker Eyert. The metal-insulator transitions of VO<sub>2</sub>: A band theoretical approach. *Annalen der Physik*, 11, July 2002.
- [46] Jamie M. Booth, Daniel W. Drumm, Phil S. Casey, Jackson S. Smith, and Salvy P. Russo. Electronic structure of tungsten-doped vanadium dioxide: from band to Mott insulator. <http://arxiv.org/abs/1507.00105>, July 2015.